Morris, J.D., Villinger, H.W., and Klaus, A. (Eds.)
Proceedings of the Ocean Drilling Program, Scientific Results Volume 205

9. SOURCE AND PETROGENESIS OF THE IGNEOUS COMPLEX CORED DURING ODP LEG 205: IMPLICATIONS FOR OFF-AXIS PLUME-RIDGE INTERACTION ON THE COCOS PLATE[1]

Brian Dreyer,[2] Valerie Chavagnac,[3] Julie Morris,[2]
and Laura Font[3,4]

ABSTRACT

New major and trace element analyses of Ocean Drilling Program Leg 170 and 205 mafic igneous samples are presented along with Sr and Nd isotopic results. Samples were cored from a sill unit (Subunit 4A) and a lower igneous unit (Subunit 4B) whose lower boundary was not drilled. The samples are dominantly microcrystalline to medium-grained glomerocrystic plagioclase-clinopyroxene gabbro in a nearly holocrystalline groundmass. Samples are dominantly low-K subalkaline tholeiites with trace element systematics that correlate with unit stratigraphy. Using isotopic data, trace element ratios little affected by fractionation, and abundance data from the least fractionated samples, it is possible to model their mantle sources and subsequent igneous processing. Melting models suggest that small differences in degrees of partial melting can generate the two geochemical groups identified within the igneous complex. Crystal fractionation and accumulation have further modified the melt compositions, particularly within the lower stratigraphic unit. Mixing models indicate that these units are derived from a mantle source that is 50%–70% enriched compared to depleted mid-ocean-ridge source mantle. In the context of the complex regional tectonic and volcanic history of the Cocos plate, this igneous complex likely represents melts of depleted upper mantle that were previously en-

---

[1] Dreyer, B., Chavagnac, V., Morris, J., and Font, L., 2006. Source and petrogenesis of the igneous complex cored during ODP Leg 205: implications for off-axis plume-ridge interaction on the Cocos plate. *In* Morris, J.D., Villinger, H.W., and Klaus, A. (Eds.), *Proc. ODP, Sci. Results,* 205, 1–38 [Online]. Available from World Wide Web: <http://www-odp.tamu.edu/publications/205_SR/VOLUME/CHAPTERS/212.PDF>. [Cited YYYY-MM-DD]

[2] Department of Earth and Planetary Sciences, Washington University, One Brookings Drive, St. Louis MO 63130, USA. Correspondence author: **dreyer@levee.wustl.edu**
[3] University of Southampton, National Oceanography Centre, Southampton, Waterfront Campus, European Way, Southampton SO14 3ZH, UK.
[4] Department of Earth Science, University of Durham, Durham DH1 3LE, UK.

Initial receipt: 22 June 2005
Acceptance: 18 January 2006
Web publication: 5 September 2006
Ms 205SR-212

riched during transit near the Galápagos hotspot. A postenrichment change in the local–regional tectonic stress regime may have triggered decompression melting and emplacement of the igneous complex far from any active spreading center or plume. Preexisting plate fractures, ridge jumps, and abandoned spreading centers may have facilitated distal reach of plume-overprinted material.

INTRODUCTION

The presence of a hotspot near a spreading center can impose large geochemical, morphological, and tectonic anomalies on lithosphere formed at mid-ocean ridges. Differences in the geochemistry of hotspot and spreading center magmas result from differences in source depth and composition. Deconvolving the causes of these geochemical anomalies in areas subject to plume-ridge interaction can help elucidate processes such as mantle source mixing, depth of melting, and tectonic and magmatic processes responsible for the surface expression of plume-ridge interaction. The proximity of the Galápagos hotspot to the Cocos-Nazca spreading center (CNS) makes this region a good natural laboratory for studies of plume-ridge interaction (Fig. F1), as the volume of published results shows (e.g., White et al., 1993; Werner et al., 1999; Hoernle et al., 2000; Harpp and White, 2001; Detrick et al., 2002; Cushman et al., 2004; Harpp et al., 2005). The products of plume-ridge interaction on the Cocos plate are subducted at the Middle American Trench (MAT) and therefore may influence the type of alteration of the subducted oceanic plate as well as the chemical composition of the mantle sources of the volcanic arc lavas (Feigenson et al., 2004).

F1. Geologic overview, p. 19.

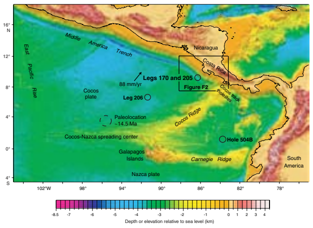

During Legs 170 and 205 of the Ocean Drilling Program (ODP), the Cocos plate was drilled across the MAT offshore of the Nicoya peninsula, Costa Rica (Kimura, Silver, Blum, et al., 1997; Morris, Villinger, Klaus, et al., 2003). Shipboard major and selected trace element analyses of igneous rocks gathered during Legs 170 and 205 suggested a Galápagos-like geochemistry rather than the expected mid-ocean-ridge basalt (MORB)–like basement above which they lie. This observation was striking, given that the location of these samples is farther north than any other igneous rock overprinted by the Galápagos hotspot. A >180-m-thick mafic igneous complex cored during these legs allows investigation of plume-ridge interaction with the expectation that geochemical variations both within these samples and in relation to regional volcanic products may reflect variations of plume-ridge interaction.

This paper uses new major and trace element analysis and isotopic data to investigate the processes of source mixing, partial melting, and fractional crystallization responsible for the generation of Leg 170 and 205 samples. We subsequently discuss the petrogenesis of the igneous complex in the context of regional tectonics and seafloor volcanism in the evolving plume-ridge system. The role of low-level off-axis volcanism and localized fluid flow within the igneous complex in modifying the shallow crustal thermal structure, in the light of recent work by Fisher et al. (2003), is discussed elsewhere (Dreyer et al., 2005).

GEOLOGICAL BACKGROUND

Tectonic Setting

The seafloor of the southernmost Cocos plate is characterized by morphological, structural, and thermal segmentation resulting from a >20-m.y. history of plume-ridge interactions and ridge jumps of the CNS. A "plate suture" exists offshore Costa Rica where lithosphere formed at the fast-spreading (~130 mm/yr full spreading rate) (Wilson, 1996) East Pacific Rise (EPR) is juxtaposed against lithosphere generated at the intermediate-spreading (65 mm/yr) (Barckhausen et al., 2001) CNS (Figs. F1, F2). Crust at the location of Legs 170 and 205 is clearly identified from the magnetic anomalies as having been generated at the EPR and as being ~24 Ma old. The initiation of CNS spreading may have occurred when a preexisting transform fault on the Farallon plate passed over the hotspot at ~24 Ma (Barckhausen et al., 2004). Crust generated at the EPR is characterized by a smooth morphology, whereas the CNS crust is morphologically irregular and has high-amplitude magnetic anomalies. The transition at this "rough/smooth" boundary (Hey, 1977) occurs in an area of abundant seamounts (~40% coverage) (von Huene et al., 1995). The spreading history of the CNS is characterized by multiple ridge jumps and migrations associated with differences in local plate motions and hotspot-induced ridge reset. The long-lived (~90 m.y.) (Hauff et al., 1997) Galápagos hotspot has continuously overprinted regional volcanic products, as evidenced in the geochemistry of the Galápagos Islands (White et al., 1993), abundant seamounts (e.g., Fisher Seamount and the Costa Rica seamount province) (Harpp and White, 2001; Werner et al., 2003), and forearc basaltic complexes in Central America (e.g., Nicoya, Osa, and Quepos) (Hauff et al., 2000). The prominent Cocos and Carnegie aseismic ridges, located on the Cocos and Nazca plates, respectively, are a consequence of the CNS location above the hotspot for at least the last 20 m.y. (Hey, 1977; Meschede and Barckhausen, 2001).

F2. Costa Rica drilling area and isochrons, p. 20.

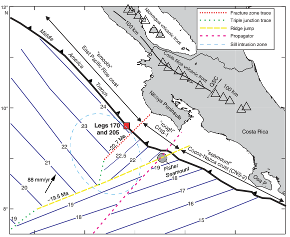

Segmentation of the Cocos plate is reflected in the structure of the overriding Caribbean plate (von Huene et al., 2000), upon which the Central American volcanic arc (CAVA) is constructed. Considerable control of Quaternary convergent margin tectonics and variable arc lava geochemistry are attributable to the subduction of different crustal types of the Cocos plate that result partly from plume-ridge interaction (Patino et al., 2000; Ranero and von Huene, 2000; von Huene et al., 2000). For example, a trench-normal fracture associated with a CNS ridge propagator (created after the CNS-1 to CNS-2, ~19.5 Ma ridge jump) (Fig. F2) continues into already subducted lithosphere (Barckhausen et al., 2001), and its landward extension coincides with an abrupt offset in the depth-to-slab beneath the CAVA called the Quesada sharp contortion (QSC) (Protti et al., 1995) (see Fig. F2 for location). The QSC also coincides with an arc gap between Arenal and Platanar-Porvenir-Poás stratovolcanoes in Costa Rica (Protti et al., 1995) and an abrupt change in the slab (sediment + oceanic basement) signal in the geochemistry of arc lavas (Carr et al., 2003, and references therein; Feigenson et al., 2004).

Igneous Stratigraphy

The Cocos plate was drilled across the MAT offshore Costa Rica during Legs 170 and 205 (Kimura, Silver, Blum, et al., 1997; Morris, Villinger, Klaus, et al., 2003). Patterns of magnetic anomalies indicate that the basement was formed at the EPR at ~24 Ma (Barckhausen et al., 2001), and precruise seismic profiles (Shipley et al., 1992) suggested a depth-to-basement of ~300 m below the seafloor/sediment interface (Fig. F3); drilling proved it to be at 378–422 m. Drilling during Leg 170 bottomed in an igneous unit after coring ~30 m at Site 1039 and 8 m at Site 1040. This igneous unit was interpreted as multiple apophyses of sill-like magma injections based on petrographic and operational data (Kimura, Silver, Blum, et al., 1997). Subsequent drilling at nearby Site 1253 (~1 km from Site 1039) during Leg 205 penetrated this unit (Subunit 4A), cored an additional 30 m of sediment, and encountered a second igneous unit (Subunit 4B). Drilling operations ended at this site after coring ~150 m of Subunit 4B without reaching its lower boundary. The recovery of igneous rocks at Site 1253 in relation to lithostratigraphic units is presented in Figure F4. Similar to Subunit 4A, Subunit 4B appears to represent a sill intrusion (see below). At Sites 1039 and 1253, the intrusion age of Subunit 4A is post-15.6–18.2 Ma derived from biostratigraphic ages of the intruded sediments (Muza, 2000). Dating is in progress for Subunit 4B.

Shipboard and postcruise thin section analyses performed on igneous rocks recovered from Legs 170 and 205 indicate that they are petrographically similar to oceanic igneous rocks cored from nearby Deep Sea Drilling Project (DSDP) Hole 504B on the Nazca plate and ODP Site 1256 on the Cocos plate (Fig. F1). Subunits 4A and 4B are microcrystalline to fine-grained and occasionally medium-grained plagioclase-clinopyroxene gabbro with plagioclase aggregates (glomerocrysts) or, more rarely, plagioclase with pyroxene aggregates in a nearly holocrystalline (microcrystalline to fine-grained, and, rarely, medium-grained) groundmass (Kimura, Silver, Blum et al., 1997; Morris, Villinger, Klaus et al., 2003). Minor primary phenocryst phases include highly altered olivine, rare orthopyroxene, ilmenite, and magnetite. Secondary phases identified by X-ray diffraction within the igneous section include zeolites, chlorite, vein-filling calcite, smectite, and products of glass alteration tentatively identified as saponite and celadonite suggesting low-temperature alteration (Kimura, Silver, Blum et al., 1997; Morris, Villinger, Klaus et al., 2003).

The crystalline texture suggests that these rocks do not necessarily preserve original melt compositions, and plagioclase growth zoning indicates magma differentiation during crystallization of phenocrysts. Phenocryst assemblages with contrasting morphologies are contained within groundmass domains of different grain-sizes, commonly separated by apparent magmatic contacts (Morris, Villinger, Klaus et al., 2003), supporting the interpretation that these subunits are multiple magma injections into partially crystallized microcrystalline gabbro.

Subunit 4A was further divided into two subunits and Subunit 4B into seven subunits based on the distribution of voids, veins, grain size variation with depth and the proportions of plagioclase to pyroxene (Morris, Villinger, Klaus, et al., 2003). Discrete alteration is greatest at the tops of the subunits and is generally higher in the lowermost cores at 1–5 vol%; some horizons in lower Subunit 4B reach nearly 50 vol% alteration. At 513 meters below the seafloor (mbsf) within Subunit 4B, a thin basaltic (cryptocrystalline) interval was recovered. Below this depth, Subunit 4B contains a higher abundance of glass and magmatic contacts, is generally more altered, and has fractures of larger size. Shipboard scientists debated the possibility that the igneous section below this horizon could be extrusive EPR oceanic crust with the overlying

F3. Migrated MCS profile and location of units, p. 21.

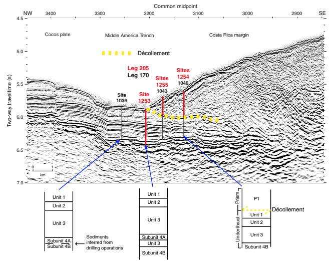

F4. Logging data and petrologic observations, p. 22.

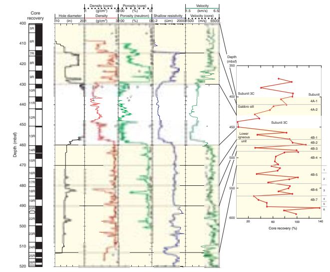

material resulting from shallow sill emplacement. Geochemical evidence presented here, however, argues that all igneous material cored during ODP Leg 205 results from magmatic overprinting of the EPR basement that was generated from an enriched source. Hydrothermal alteration and implications of fluid flow within Subunit 4B are discussed elsewhere (Dreyer et al., 2005).

ANALYTICAL METHODS

Previously published geochemical data of Subunits 4A and 4B include onboard X-ray fluorescence (XRF) (Leg 170) and inductively coupled plasma–atomic emission spectroscopy (ICP-AES) (Leg 205) analyses of a total of 52 samples for major and selected trace elements (Kimura, Silver, Blum, et al., 1997; Morris, Villinger, Klaus, et al., 2003). An additional 50 samples were powdered in an alumina ball mill and analyzed by XRF, inductively coupled plasma–mass spectrometry (ICP-MS), and instrumental neutron activation analysis (INAA) at Washington University in St. Louis (Missouri, USA). Results are reported here. A total of 33 samples from Leg 205 were analyzed for Sr and Nd isotopes by thermal ionization mass spectrometry (TIMS) at the National Oceanography Centre, Southampton (UK).

Major Elements

XRF

Major elements were determined for 34 samples from Leg 205 at Washington University by XRF analysis of fused glass discs prepared from preignited sample powders, using procedures described by Couture et al. (1993). Loss on ignition (LOI) values represent mass loss measured on sample powders ignited for 50 min at 950°C in a muffle furnace. LOI was <0.5 wt% for most samples but was 0.91–1.46 wt% for samples with Mg# (= $Mg^{2+}/[Mg^{2+} + Fe^{2+}]$, where Fe_2O_3 is converted to FeO) >0.58 (one exception), which are clustered at the top half of Subunit 4B (~460–509 mbsf). Average sum of element oxides is 99.6 wt%, with all but three samples having totals between 99.5 and 100.5 wt%. Analyses of the reference basalts BHVO-2 and BIR-1 and gabbro JGB-1 agree with certified values within 1 or 2 σ, except for the low values (<0.05 wt%) of K_2O and P_2O_5 in BIR-1 (Tables T1, T2).

T1. Analysis of standard reference materials, p. 33.

Trace Elements

ICP-MS

T2. XRF and ICP-MS analysis, p. 35.

Trace element abundances were analyzed by high-resolution ICP-MS (Table T2). Powders of rock samples and geochemical reference standards were dissolved with 5:1 HF:HNO_3 in a microwave-assisted digestion system. Solutions were diluted with 1% trace metal grade HNO_3 to attain a sample mass:dilution ratio of ~1:1000. For analysis of Sr, Ba, Y, and selected transition row metals, samples were further diluted to 1:5000 to reduce concentrations enough to preserve detection in pulse counting mode.

Instrument calibration for rare earth elements (REEs) and high-field-strength elements (HFSEs) (Zr, Hf, Nb, Ta, U, and Th) is performed using a rock reference standard solution, and the regression is forced through the origin after blank subtraction. This is a reliable method given the >6 orders of magnitude dynamic linear range of the ICP-MS (Jarvis et al., 1992; Eggins et al., 1997). Calibration with geochemical reference standards maintains approximately constant matrix conditions, including the presence of residual trace HF from sample digestion (McGinnis et al., 1997), and mitigates many of the issues created using calibration with near matrix-free synthetic cocktails of high-field-strength single-element standards. Elements that are not appreciably affected by oxide interferences and easily rinsed with a few percent HNO_3 are calibrated against synthetic multielement solutions created from single-element standards. The choice of geochemical reference standards for some elements and synthetic calibration standards for others was made after extensive testing of both approaches. External oxide correction for the REEs Eu-Lu and HFSEs Hf and Ta is performed offline following methods modified from Lichte et al. (1987). Initial oxidation formation factors range from ~3% to <0.5% for the REEs, depending on element. In-run measurement of ThO/Th during analysis monitors changes in oxide formation and allows sample-to-sample oxide correction (Lichte et al., 1987); REE + Th oxide formation is approximately linear run to run ($R^2 > 0.97$).

Typical instrument runs include measurements of procedural blanks, geochemical reference standards, and a drift solution interspersed frequently with sample solutions. Accuracy and precision based on replicate measurements of appropriate geochemical reference standards JGb-1 and BIR-1 are shown in Table T1.

INAA

Trace elements for 16 samples from Leg 170 (12 from Site 1039 and 4 from Site 1040) were measured by INAA at Washington University in St. Louis (Table T3). Powdered rock chips were encapsulated in high-purity silica tubing and subsequently irradiated at the University of Missouri research reactor in a thermal neutron flux of 5.15×10^{13} cm/s. Samples were radioassayed by gamma ray spectroscopy following the methods of Korotev (1996), and data were reduced using an updated version of the TEABAGS (trace element analysis by automated gamma ray spectroscopy) software developed by Lindstrom and Korotev (1982). Estimated accuracy and 1-σ precision for standard reference material JGb-1 is given in Table T1.

T3. INA analysis, p. 38.

Comparison of Multiple Data Sets

The coherence of data measured by multiple analytical techniques was evaluated by comparing ongoing, long-term analyses of standard reference materials at Washington University in St. Louis. Analyses of repeated determinations of reference basalts BCR-1 and NBS-688 by XRF and INAA methods at Washington University (Korotev, 1996; Couture et al., 1993) are in excellent agreement with certified values. Several trace elements of reference basalt JGb-1 have also been measured by both INAA and ICP-MS at Washington University and agree within 2-σ error (Table T1).

RESULTS

Samples analyzed from Legs 170 and 205 are characterized by small variations in major element oxide composition typical for ocean floor igneous rocks (Tables T2). These samples are low- to medium-K (0.07–0.53 wt%) subalkalic rocks of basaltic composition (Fig. F5) and show a Fe-enrichment trend characteristic of mid-ocean-ridge tholeiites (Fig. F6). All samples contain between 46 and 50 wt% SiO_2 with Mg# ranging from 0.44 to 0.63 and have therefore experienced a significant degree of fractionation. Samples from the Leg 205 Hole 1253A interval ~460–509 mbsf (Subunits U4B-1–U4B-4) generally have larger proportions of pyroxene to plagioclase phenocrysts (Morris, Villinger, Klaus, et al., 2003) and higher whole-rock Mg# (0.58–0.63) than Subunit 4A and the lower part of Subunit 4B (0.48–0.57).

Overall LOI is low (–0.12 to 1.46 wt%), consistent with the low degree of alteration of these samples. The abundances of fluid-mobile trace elements (Cs, Sb, Pb, Li, Rb, Ba, and Sr) vary downhole, especially near subunit boundaries. The samples with the highest abundance of these elements generally have an elevated $^{87}Sr/^{86}Sr$ ratio, which also correlates with ratios of fluid mobile/immobile trace elements and generally occur near subunit boundaries (Chavagnac et al., in prep). This suggests that geochemical modification may have accompanied localized seawater interaction. Trends in major and compatible trace element abundances are consistent with phase equilibria control by olivine, plagioclase, clinopyroxene, and Fe-Ti oxides, all of which are phenocrysts, although olivine is rare (Morris, Villinger, Klaus et al., 2003). A combination of fractionation and alteration processes cannot encapsulate all variations in major and compatible trace elements of Subunits 4A and 4B. For example, Figure F7 shows the covariation of V and Ti within Subunits 4A and 4B. The positive linear variation reflects enrichment in the magma during fractional crystallization, but the offset trends (Subunit 4A shifted to higher TiO_2) suggest that the units are not derived from a common melting event.

The two stratigraphic Subunits 4A and 4B form distinct geochemical groups that can be distinguished by abundances and ratios of fluid-immobile incompatible trace elements that are minimally affected by secondary alteration. Despite similar ranges in SiO_2 and Mg# for both units, the abundances of fluid-immobile incompatible trace elements (La, Zr, Nb, Hf, and Th) are generally higher in the upper igneous Subunit 4A. This bimodal distribution is more clearly developed in ratios of immobile, incompatible trace elements that are not controlled by degree of fractionation as gaged by Mg# (Fig. F8).

The distinct groups are also apparent in the REE abundances of the Leg 170 and 205 igneous rocks (Fig. F9). The upper Subunit 4A is characterized by a tight range in abundances, with light rare earth elements (LREEs) ~50–60× chondrites and heavy rare earth elements (HREEs) ~15× chondrites. Subunit 4B has a range of LREE (15–30×) and HREE (7–15×) concentrations. Patterns for Subnit 4B are nearly parallel, and lower REE abundances correlate generally, though not systematically, with higher Mg#. Samples from Subunit 4A are characterized by higher LREEs than Subunit 4B, with partly overlapping HREE abundances. Normalized REE abundances of the Leg 170 and 205 igneous rocks lie almost entirely within the combined fields of regional spreading center (EPR and CNS) and Galápagos Islands basalts. REE patterns of the samples are distinct from spreading center basalts, having lower HREE and

F5. Total alkalis vs. SiO_2, p. 23.

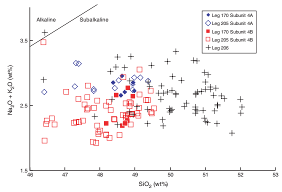

F6. AFM diagram, p. 24.

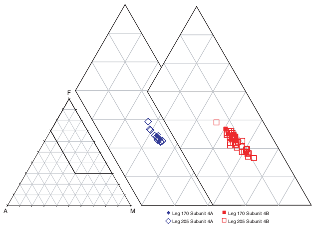

F7. V vs. TiO_2, p. 25.

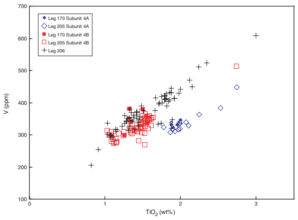

F8. Selected minor and trace element ratios vs. Mg#, p. 26.

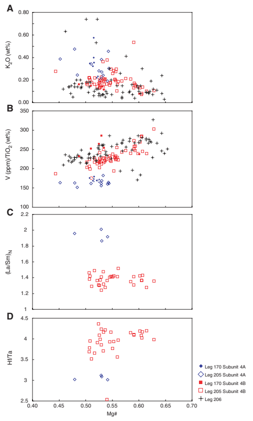

higher LREE abundance patterns, and are more similar to moderately enriched basalts of the Galápagos Islands.

F9. Chondrite-normalized REE diagram, p. 28.

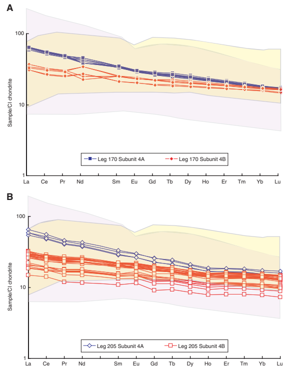

DISCUSSION

Mantle Source and Mixing Relationships

Sr and Nd Isotopes

The compositional ranges of regional hotspot-related volcanic products have been attributed to mixing of three or more end-members in addition to a depleted MORB source (White et al., 1993; Kurz and Geist, 1999; Harpp and White, 2001; Blichert-Toft and White, 2001; Harpp et al., 2005). One end-member (most prevalent in lavas from the Wolf-Darwin Lineament) accounts exclusively for elevated Pb isotope systematics but a small amount of total variation (3.3%) (Harpp and White, 2001; Harpp et al., 2005). As this data set does not yet exist for our samples, the remaining regional geochemical end-members reduce to (1) depleted, MORB source; (2) enriched, plume source; and (3) elevated incompatible trace element (ITE), Sr radiogenic (Bow, 1978; Bow and Geist, 1992; Geist, 1992; Graham et al., 1993; Harpp and White, 2001; Blichert-Toft and White, 2001). The locus of this last potential end-member ("FLO" of Harpp and White, 2001) is thought to be beneath Isla Floreana in the southern Galápagos archipelago, but it may not represent a signal of the plume (Kurz and Geist, 1999).

Neodymium isotopes are used here to help constrain mixing relationships between the aforementioned geochemical mantle end-members and as a prerequisite for the identification of reasonable parental trace element composition that will, in turn, be used to model petrogenesis. Figure **F10** plots Sr-Nd isotopic values of samples from Subunits 4A and 4B from Leg 205 and fields of the EPR, CNS, and the Galápagos Islands, along with tholeiitic seamounts north of the Cocos Ridge axis proximal to the locations of Legs 170 and 205. The restricted range in Nd isotopes (0.512937–0.512974, *N* = 25; one value extends to 0.513020) indicates that Subunits 4A and 4B sample an approximately uniform $^{143}Nd/^{144}Nd$ source despite the wide regional isotopic variation. This mantle source is more isotopically enriched (less radiogenic Nd) than that of EPR MORB and is likely a mixture of more and less enriched mantles, similar to the source for the Galápagos Islands, regional seamounts, and the Cocos and Carnegie Ridges (White et al., 1993; Hoernle et al., 2000, 2002; Harpp and White, 2001; Harpp et al., 2005). The overlapping fields suggest widespread mixing, as has been argued previously for the CNS (White et al., 1993; Hoernle et al., 2000). An extended discussion on the relationship between the enriched signatures of Subunits 4A and 4B with those of seamounts on the flanks of the EPR existing far from plume influence (Nui and Batiza, 1997; Nui et al., 2002) is beyond the scope of this paper. However, a link between Subunits 4A and 4B and the Galápagos hotspot is suggested from geochemical similarities and the proximity of the hotspot and the paleolocation of emplacement. Though not conclusive in resolving the source of enrichment, we note that the $^{143}Nd/^{144}Nd$ ratios of Subunits 4A and 4B (only one value above 0.513000) are more enriched than the vast majority of EPR flank seamount lavas ($^{143}Nd/^{144}Nd$ = 0.512956–0.513183) (Nui et al., 2002).

F10. $^{143}Nd/^{144}Nd$ vs. $^{87}Sr/^{86}Sr$, p. 29.

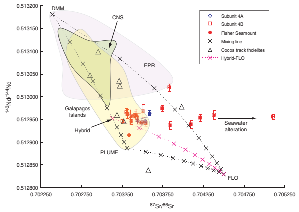

Assuming that elevated (higher ^{87}Sr/^{86}Sr) ratios seen in Leg 205 samples is due to seawater interaction, and therefore not primary, Nd isotopes are used to calculate mixing proportions between depleted MORB mantle and the enriched Galápagos end-member. The majority of Leg 205 samples are derived from a mantle source that is 50%–70% enriched; one sample requires ~30% enrichment to explain elevated ^{144}Nd/^{144}Nd = 0.513020. If the mantle source is isotopically homogeneous as argued, then variations observed in minor and fluid-immobile incompatible trace elements are most likely due to differences in degrees of partial melting and/or fractional crystallization. The premise that elevated Sr isotope values are due to seawater interaction rather than admixture of the FLO end-member is supported by several independent lines of evidence. Most Sr isotope excursions are correlated with increased ratios of fluid-mobile:less-fluid-mobile trace elements and measurements of increased fracture density (**Pfender and Villinger,** this volume; Chavagnac et al., in prep), suggesting a secondary origin. The trend of Leg 205 Sr-Nd isotopes is primarily horizontal toward elevated Sr isotopic values with very limited variation in Nd isotopic values. This is in contrast with trends predicted by modeling mixing of the FLO end-member with a uniform mantle source, itself composed of depleted MORB and enriched plume components. Furthermore, ^{87}Sr/^{86}Sr values of several samples extend beyond the range of values expected from a three-component mixture (Fig. **F10**). We conclude that compositions of Leg 205 samples are dominated by binary mixing of enriched and depleted sources; this question will be revisited with trace elements.

Trace Elements

F11. $(La/Sm)_N$ vs. Hf/Ta, p. 30.

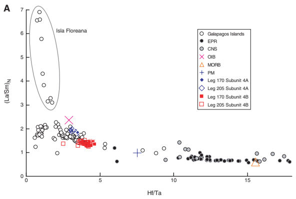

Regional geochemical end-members have characteristic trace element abundances. Figure **F11A** plots data from regional basalts and illustrates end-member mixing relationships in terms of ratios of chondrite-normalized $(La/Sm)_N$ vs. Hf/Ta, forming the hyperbolic "mantle mixing" trend. Samples from Subunits 4A and 4B are well separated; ratios of additional immobile incompatible elements (e.g., Nb/Y and Zr/Y) give similar results. Generally, Subunit 4A has $(La/Sm)_N$ >1.75 and Hf/Ta <3.5, and samples from Subunit 4B have $(La/Sm)_N$ <1.5 and Hf/Ta >3.5, with the exception of one sample (Hf/Ta ~2.5). Leg 170 and 205 samples cluster toward the enriched end-member and lie within a field outlined by the Galápagos Islands. Samples from the "main series" from Isla Floreana of the Galápagos Islands trend toward anomalously high $(La/Sm)_N$, the locus of proposed ITE-rich FLO end-member. Melt modeling, presented in detail in the following section, shows that increasingly small degrees of partial melting of a hybrid mixture of enriched and depleted sources would approach the high $(La/Sm)_N$, low Hf/Ta of the ITE-rich Isla Floreana samples, but melt processes alone are unable to explain the distinctive isotope systematics of this end-member (namely, high ^{206,208}Pb/^{204}Pb, high ^{87}Sr/^{86}Sr, low ^{143}Nd/^{144}Nd, and relatively high ^{176}Hf/^{177}Hf) (cf. Kurz and Geist, 1999). Variable decoupling between isotopes and ITE ratios during igneous processing of Galápagos hotspot products is discussed in Harpp et al, (2005). Without more definitive Pb and Hf isotope data, we tentatively conclude that the FLO end-member is not a significant component in the source of Leg 170 and 205 samples and have instead focused, therefore, on two-component mixing between enriched and depleted end-members. In sum, both Nd isotopes and ratios of ITEs indicate that source mixing is an important process in both Leg 170 and 205 samples. Overlap of some samples from the Galápagos Islands with a few of the most enriched CNS and EPR basalts, observed with both isotope (Fig. **F10**) and trace element systematics (Fig. **F11A**), suggests regional influence of the plume and smearing of the source signals (cf. White et al., 1993; Harpp and White, 2001; Blichert-Toft and White, 2001, and references therein).

In the binary Sr-Nd isotope mixing model presented above, we assumed that the enriched and depleted mantle end-members mix as solid materials. We have also examined the possibility that one or both of the parental sources of Subunits 4A and 4B magmas were melts themselves, in which case the resulting mixing proportions and trace element compositions will differ. To test these possibilities we also modeled (1) an enriched melt mixing with solid depleted ambient mantle and (2) an enriched melt mixing with a depleted melt. Because an enriched melt will have comparatively large abundance of trace elements, admixture of this end-member is highly restricted because the resultant hybrid magma must ultimately reproduce observed Nd isotope values. In this case, Leg 205 samples would represent a mixture of ~5% enriched melt with 95% depleted ambient mantle. In the second case of an enriched melt mixing with a depleted melt, resultant mixing *proportions* change only modestly compared to solid-source mixing if extents of melting are less than a few percent for both enriched and depleted sources. In this scenario, Leg 205 samples would represent 30%–50% enrichment over ambient depleted mantle, as approximated by average oceanic island basalt (OIB) and MORB of Sun and McDonough (1989). In both cases, subsequent modeling of reasonable degrees of melting and crystallization cannot reproduce the observed range in ITE abundances and ratios of Subunits 4A and 4B. Therefore, we consider these scenarios unlikely compared to solid source mixing, which is discussed in the next section.

Petrogenesis

Partial Melting

Given the approximately uniform Nd isotope source of Subunits 4A and 4B, variable degrees of partial melting and fractional crystallization are potential causes of their observed geochemical variation. Melt generation models using ratios of incompatible trace elements are examined in conjunction with previously established end-member mixing proportions to deconvolve the roles of source mixing and subsequent igneous processing. In the following sections, we evaluate these combined functions in the generation of the distinct trace element compositions of Subunits 4A and 4B. Figure **F11B** superimposes models of binary mixing, partial (batch) melting of ~60% enriched source, and subsequent fractional crystallization (see **"Fractional Crystallization and Crystal Accumulation,"** p. 11) with data from Subunits 4A and 4B as well as regional basalts; Plank and Langmuir (1992) demonstrate that batch melting closely reproduces a diverse range of complex melting mechanisms and approximate the net effects of the melting process remarkably well.

The data for Subunits 4A and 4B plot along or near the modeled partial melting curves and at higher $(La/Sm)_N$ and lower Hf/Ta of the modeled mantle (PLUME-DMM) mixing trend. Both garnet and garnet-free (spinel) source mineralogies were considered, which may affect fractionation within the REEs and Hf from Ta during partial melting because of their contrasting incompatibilities in the presence of garnet. Additional melt modeling (not shown) using the REE concentrations of Subunits 4A and 4B indicates that a small, early formed proportion of the total melt occurring in the presence of garnet can transmit the characteristic slope of the HREE to the subsequent melts. Although published melting models for the vast majority of Galápagos Island seamounts and the Cocos and Carnegie Ridges (Harpp and White, 2001; Harpp et al., 2005) indicate the majority of melting in the presence of garnet, the gentle slope of normalized HREE patterns for both Subunits 4A and 4B suggests that the bulk of melting did not occur in the garnet stability field (i.e., >60 km) (Fig. F9).

Combined results suggest that the majority of Subunit 4A and 4B samples are adequately explained by 2%–7% partial melting of a hybrid source containing 50%–70% of the enriched end-member (Fig. F11B; see caption for model details). Furthermore, Subunit 4A is distinguished from Subunit 4B by lower degrees of partial melting; a difference of at least 2% melting separates Subunit 4A from Subunit 4B (Fig. F11B). Offset linear trends of V vs. TiO_2 (Fig. F7) and variable ITE ratios (such as Hf/Ta) (Fig. F8) at similar Mg# are also consistent with variations in degree of partial melting. More sophisticated models of polybaric partial melting that consider the compositional dependence of partition coefficients have yet to be applied, but it appears that Subunits 4A and 4B are not associated with extensive melting at lithospheric levels deeper than typical MORB despite geochemical evidence for hotspot overprinting. These conditions place limitations on melt generation in proximity to the plume (see **"Models of Sill Emplacement,"** p. 12). In the next section, we discuss the causes of variable trace element abundances within the igneous units.

Fractional Crystallization and Crystal Accumulation

Petrologic relations and geochemical variation within Subunits 4A and 4B indicate that they are likely to have experienced a significant degree of fractional crystallization. Previously, we have shown that the isotopic and ITE ratio compositions of the majority of Leg 170 and 205 samples can be modeled with a restricted range of mantle mixing and melting. These geochemical parameters were chosen, in part, based on their relative insensitivity to the degree of shallow fractional crystallization. Models indicate that reasonable degrees of fractional crystallization of basaltic liquids are not responsible for the observed differences in ITE ratios between Subunits 4A and 4B (Fig. F11B, inset). For example, 50% modal fractional crystallization from a basaltic melt results in an increase of La/Sm of ~3% in the remaining melt, whereas the minimum difference between Subunits 4A and 4B is ~20%. However, a twofold range in the abundances of the REE with similarly shaped patterns is evidence of additional variation with Subunit 4B, which we relate to the effects of fractional crystallization and crystal accumulation.

In the preceding discussion, we have shown that the majority of samples are modeled as a partial melts of a mixture of enriched and depleted mantle sources. These melts produce magmas with elevated REE abundances, adequately matching compositions observed in the majority of samples from Subunits 4A and 4B. However, Subunit 4B samples with the lowest REE abundance cannot be reconciled without additional consideration. We suggest that the compositional differences within Subunit 4B can be related by crystal accumulation. As envisioned, ITE-rich melts are effectively "diluted" by the addition of variable amounts of early-formed fractionates that are relatively ITE poor (Fig. F12). Whole-rock geochemical data are used to place plausible constraints on this process. We are able to reproduce the entire REE abundance range of Subunit 4B by adding increments of an instantaneous fractionating phase assemblage to the Subunit 4B sample with the highest REE abundance. The modeled fractionating phase assemblages (plagioclase = 0.57; clinopyroxene = 0.25; olivine = 0.09; orthopyroxene = 0.08; magnetite = 0.01) are consistent with approximate modal abundances within Leg 170 and 205 samples. The La/Sm ratio of the modeled bulk partition coefficient is 1.3, indicating that little LREE fractionation would occur during this relatively small interval of crystallization (Mg# = 0.63–0.51). This is consistent with the observed $(La/Sm)_N$ ratios of Subunit 4B samples (1.24–1.51). Samples with the lowest REE abundance occur within the interval 460–509 mbsf and exhibit the highest whole-rock Mg# and most positive Eu anomalies (up to Eu/Eu* = 1.15), which may be consistent with these samples having a higher proportion of earlier formed minerals. However, there are no reports of a distinct change in the crystallinity or modal mineralogy from onboard visual core descriptions of this interval (Morris, Villinger, Klaus, et al., 2003), suggesting that the differences in the bulk compositions may be due to variations in mineral chemistry rather than mode. Without geochemical analyses of individual phenocrysts we are unable to more quantitatively model this process.

F12. Crystal accumulation model, p. 32.

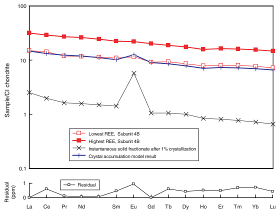

Models of Sill Emplacement

Geochemistry and tectonics together provide constraints on mechanisms for sill emplacement and its regional impact. Trace element and Nd isotope systematics indicate that both subunits cored during Legs 170 and 205 share geochemical similarities with other volcanic products of the Galápagos hotspot. At the time of intrusion, after 15.6–18.2 Ma, the paleolocation of Subunit 4A was quite distant from both the EPR (~400 km) and the CNS (~140 km) (Fig. F1). Distal off-axis emplacement is unlikely because morphological, petrographic, and geochemical studies of the EPR show that the vast majority of off-axis volcanism occurs within ~10 km of the axis (Wilson, Teagle, Acton, et al., 2003; Reynolds and Langmuir, 2000; Sims et al., 2003), although some melt production extends >100 km from the fast-spreading EPR axis at 17°–19°S (Scheirer et al., 1998). Although precise ages are yet unknown, existing petrographic and geochemical similarities imply a link between Subunits 4A and 4B, which are unlikely to represent true EPR basement. Similarly, at its nearest point to the Galápagos hotspot at 14–12 Ma, the paleolocation of Legs 170 and 205 was still *several hundred* kilometers to the northwest (see Meschede and Barckhausen, 2000, 2001; Harpp et al., 2005) (Fig. F1). If Subunits 4A and 4B are related to the Galapagos hotspot, then it is likely that they are far-field manifestations of plume-ridge interaction.

A possible explanation for the age-location relationship of the igneous complex is distal emplacement of a melt originating near the hotspot. As envisioned, preexisting lithospheric weakness resulting from the initial fracture of the Farallon plate and/or prior ridge jumps on the CNS may have permitted enhanced plume influence at greater distances. A similar scenario may explain a series of alkalic and tholeiitic OIB-like ~14-Ma seamounts that are clustered north of the Cocos Ridge near an extinct spreading center of the CNS (Barckhausen et al., 2001), and this age is consistent with an intrusion age after 15.6–18.2 Ma for Subunit 4A. Geochemical constraints based on mixing and melting models discussed above restrict this style of (enriched) melt-induced mixing with ambient MORB-source mantle and argue instead for solid source mixing prior to melting.

Alternatively, the generation and emplacement of the Leg 170 and 205 igneous complex may involve melting of upper mantle that was previously enriched. This enrichment could exist as Galápagos plume material entrained within the ambient depleted mantle. An age of 8–10 Ma brackets a high-amplitude seismic reflector associated with widespread deformation of the Cocos plate called the sill intrusion zone, which includes the locations of Leg 170 and 205 (Silver et al., 2004) (Fig. F2). Although controversy surrounds the cause of the deformation, this age may be coincident with the Cocos Ridge collision with the MAT (Abratis and Woerner, 2001, but cf. Graefe et al., 2002), leading to the development of a stress regime that may have fostered renewed decompression melting on a local to regional scale. Such a scenario is consistent with a recently published model by Harpp et al. (2005) regarding the tectonic-petrogenetic formation of the Cocos and Carnegie Ridges and associated seamounts. This model suggests that postabandonment alkalic and tholeiitic volcanism immediately followed and was probably caused by either a ridge jump or rift failure and not the direct activity of the Galápagos hotspot.

CONCLUSIONS

The microcrystalline to medium-grained plagioclase-clinopyroxene igneous units cored during Legs 170 and 205 are low- to medium-K subalkaline tholeiites; trace element systematics distinguish two geochemical groups that are also stratigraphically separated as Subunits 4A and 4B. Models of mixing between regional geochemical end-members indicate that these sills are 50%–70% enriched compared to depleted MORB-source mantle. Models suggest that small differences in degrees of partial melting (2.5%–3.5% vs. 5%–7%) can explain the distinct geochemical groups. Geochemical variability in the lower Subunit 4B is consistent with modest amounts of fractional crystallization and/or crystal accumulation.

Within the context of the complex regional tectonic and volcanic history of the Cocos plate, the igneous complex likely represents melts of upper mantle that was previously close to, but not above, the Galápagos hotspot. Fractures, ridge jumps, and abandoned spreading centers on the southern Cocos plate could be related to proximity of the plume (Barckhausen et al., 2001). These lithospheric weaknesses may have facilitated distal reach of material overprinted by the plume. This material was likely melted subsequent to the time of enrichment at intermediate depths less than those of garnet stability (i.e., <60 km). A change in tectonic stresses associated with subduction of the irregular lithosphere of the southern Cocos plate may have facilitated local decompression melting and emplacement.

ACKNOWLEDGMENTS

This research used samples and data provided by the Ocean Drilling Program (ODP). The ODP is sponsored by the U.S. National Science

Foundation (NSF) and participating countries under management of Joint Oceanographic Institutions (JOI), Inc. Funding for this research was provided by the U.S. Science Support Program. Randy Korotev is thanked for his assistance with INAA. This work was supported in part by the US Department of Energy (DOE) reactor sharing program at the University of Missouri Research Reactor (MURR). We are grateful to Folkmar Hauff, Holger Paulick, an anonymous reviewer, and the ODP editorial staff for their thoughtful comments, which significantly improved the manuscript.

REFERENCES

Abratis, M., and Woerner, G., 2001. Ridge collision, slab-window formation, and the flux of Pacific asthenosphere into the Caribbean realm. *Geology,* 29(2):127–130. **doi:10.1130/0091-7613(2001)029<0127:RCSWFA>2.0.CO;2**

Agee, C.B., 1990. A new look at differentiation of the Earth from melting experiments on the Allende meteorite. *Nature (London, U. K.),* 346:834–837. **doi:10.1038/346834a0**

Barckhausen, U., Ranero, C.R., von Huene, R., Cande, S.C., and Roeser, H.A., 2001. Revised tectonic boundaries in the Cocos plate off Costa Rica: implications for the segmentation of the convergent margin and for plate tectonic models. *J. Geophys. Res.,* 106:19207–19220. **doi:10.1029/2001JB000238**

Barckhausen, U., Ranero, C.R., and Weinrebe, W., 2004. Did the Cocos-Nazca spreading center form at a transform fault during Farallon plate break-up? *Eos, Trans. Am. Geophys. Union,* 85:T41A-1166. (Abstract)

Blichert-Toft, J., and White, W.M., 2001. Hf isotope geochemistry of the Galápagos Islands. *Geochem., Geophys., Geosyst.,* 2(9). **doi:10.1029/2000GC000138**

Bow, C.S., 1978. Petrogenesis of basanitoid lavas from Floreana Island, Galápagos: an example of partial melting of a light-rare-earth-enriched source? *Geol. Soc. Am. Bull.,* 10(7):370.

Bow, C.S., and Geist, D.J., 1992. Geology and petrology of Floreana Island, Galápagos archipelago, Ecuador. *J. Volcanol. Geotherm. Res.,* 52:83–105. **doi:10.1016/0377-0273(92)90134-Y**

Carr, M.J., Feigenson, M.D., Patino, L.C., and Walker, J.A., 2003. Volcanism and geochemistry in Central America: progress and problems. *In* Eiler, J. (Ed.), *Inside the Subduction Factory.* Geophys. Monogr., 138.

Couture, R.A., Smith, M.S., and Dymek, R.F., 1993. X-ray fluorescence analysis of silicate rocks using fused glass discs and a side-window Rh source tube: accuracy, precision and reproducibility. *Chem. Geol.,* 110:315–328. **doi:10.1016/0009-2541(93)90326-E**

Cushman, B., Sinton, J., Ito, G., and Eaby Dixon, J., 2004. Glass compositions, plume-ridge interaction, and hydrous melting along the Galápagos spreading center, 90.5°W to 98°W. *Geochem., Geophys., Geosyst.,* 5:Q08E17. **doi:10.1029/2004GC000709**

DeMets, C., Gordon, R.G., Argus, D.F., and Stein, S., 1990. Current plate motions. *Geophys. J. Internat.,* 101:425–478.

Detrick, R.S., Sinton, J.M., Ito, G., Canales, J.P., Behn, M., Blacic, T., Cushman, B., Dixon, J.E., Graham, D.W., and Mahoney, J.J., 2002. Correlated geophysical, geochemical, and volcanological manifestations of plume-ridge interaction along the Galápagos spreading center. *Geochem., Geophys., Geosyst.,* 3(10):8501. **doi:10.1029/2002GC000350**

Dreyer, B., Chavagnac, V., and Morris, J., 2005. Low temperature fluid flow in the permeable igneous complex of the subducting Cocos plate, offshore Costa Rica. *Eos, Trans. Am. Geophys. Union,* 86(52)(Suppl.):T33A-0515. (Abstract)

Eggins, S.M., Woodhead, J.D., Kinsley, L.P.J., Mortimer, G.E., Sylvester, P., McCulloch, M.T., Hergt, J.M., and Handler, M.R., 1997. A simple method for the precise determination of ≥40 trace elements in geological samples by ICPMS using enriched isotope internal standardisation. *Chem. Geol.,* 134:311–326. **doi:10.1016/S0009-2541(96)00100-3**

Feigenson, M.D., Carr, M.J., Maharaj, S.V., Juliano, S., and Bolge, L.L., 2004. Lead isotope composition of Central American volcanoes: influence of the Galápagos plume. *Geochem., Geophys., Geosyst.,* 5(6):Q06001. **doi:10.1029/2003GC000621**

Fisher, A.T., Stein, C.A., Harris, R.N., Wang, K., Silver, E.A., Pfender, M., Hutnak, M., Cherkaoui, A., Bodzin, R., and Villinger, H., 2003. Abrupt thermal transition reveals hydrothermal boundary and role of seamounts within the Cocos plate. *Geophys. Res. Lett.,* 30(11). **doi:10.1029/2002GL016766**

Geist, D.J., 1992. An appraisal of melting processes and the Galápagos hotspot: major- and trace- element evidence. *J. Volcanol. Geotherm. Res.,* 52:65–82. **doi:10.1016/0377-0273(92)90133-X**

Graefe, K., Frisch, W., Villa, I.M., and Meschede, M., 2002. Geodynamic evolution of southern Costa Rica related to low-angle subduction of the Cocos Ridge: constraints from thermochronology. *Tectonophysics,* 348(4):187–204. **doi:10.1016/S0040-1951(02)00113-0**

Graham, D.W., Christie, D.M., Harpp, K.S., and Lupton, J.E., 1993. Mantle plume helium in submarine basalts from the Galápagos platform. *Science,* 262:2023–2026.

Guevara, M., Verma, S.P., and Velasco-Tapia, F., 2001. Evaluation of GSJ intrusive rocks JG1, JG2, JG3, JG1a, and JGb1 by an objective outlier rejection statistical procedure: Revista Mexicana de Ciencias. *Geologicas,* 18:74–88.

Harpp, K.S., Wanless, V.D., Otto, R.H., Hoernle, K., and Werner, R., 2005. The Cocos and Carnegie aseismic ridges: a trace element record of long-term plume-spreading center interaction. *J. Petrol.,* 46(1):109–133. **doi:10.1093/petrology/egh064**

Harpp, K.S., and White, W.M., 2001. Tracing a mantle plume: isotopic and trace element variations of Galápagos seamounts. *Geochem., Geophys., Geosyst.,* 2(6). **doi:10.1029/2000GC000137**

Hauff, F., Hoernle, K., Schminke, H.-U., and Werner, R., 1997. A mid-Cretaceous origin for the Galapagos hotspot: volcanological, petrological, and geochemical evidence from Costa Rican oceanic crustal segments. *Geol. Rundsch.,* 86(1):141–155. **doi:10.1007/PL00009938**

Hauff, F., Hoernle, K., van den Bogaard, P., Alvarado, G., and Garbe-Schoenberg, D., 2000. Age and geochemistry of basaltic complexes in western Costa Rica: contributions to the geotectonic evolution of Central America. *Geochem., Geophys., Geosyst.,* 1(5). **doi:10.1029/1999GC000020**

Hey, R., 1977. Tectonic evolution of the Cocos-Nazca spreading center. *Geol. Soc. Am. Bull.,* 88:1404–1420. **doi:10.1130/0016-7606(1977)88<1404:TEOTCS>2.0.CO;2**

Hoernle, K., van den Bogaard, P., Werner, R., Lissinna, B., Hauff, F., Alvarado, G., and Garbe-Schoenberg, D., 2002. Missing history (16–71 Ma) of the Galápagos hotspot: implications for the tectonic and biological evolution of the Americas. *Geology,* 30(9):795–798. **doi:10.1130/0091-7613(2002)030<0795:MHMOTG>2.0.CO;2**

Hoernle, K., Werner, R., Phipps Morgan, J., Garbe-Schoenberg, D., Bryce, J., and Mrazek, J., 2000. Existence of complex spatial zonation in the Galápagos plume. *Geology,* 28:435–438. **doi:10.1130/0091-7613(2000)028<0435:EOCSZI>2.3.CO;2**

Jarvis, K.E., Gray, A.L., and Houk, R.S., 1992. *Handbook of Inductively Coupled Plasma Mass Spectrometry:* New York (Chapman and Hall).

Kimura, G., Silver, E.A., Blum, P., et al., 1997. *Proc. ODP, Init. Repts.,* 170: College Station, TX (Ocean Drilling Program). [**HTML**]

Kinzler, R.J., 1997. Melting of mantle peridotite at pressures approaching the spinel to garnet transition: application to mid-ocean ridge basalt petrogenesis. *J. Geophys. Res., [Solid Earth],* 102:853–874. **doi:10.1029/96JB00988**

Korotev, R.L., 1996. A self-consistent compilation of elemental concentration data for 93 geochemical reference samples. *Geostand. Newsl.,* 20:217–245.

Kurz, M.D., and Geist, D., 1999. Dynamics of the Galápagos hotspot from helium isotope geochemistry. *Geochim. Cosmochim. Acta,* 63(23–24):4139–4156. **doi:10.1016/S0016-7037(99)00314-2**

Lichte, F.E., Meier, A.L., and Crock, J.G., 1987. Determination of the rare earth elements in geological materials by inductively coupled plasma mass spectrometry. *Anal. Chem.,* 59:1150–1157. **doi:10.1021/ac00135a018**

Lindstrom, D.J., and Korotev, R.L., 1982. TEABAGS: computer programs for instrumental neutron activation analysis. *J. Radioanal. Chem.,* 70:439–458.

Lodders, K., and Fegley, B., Jr., 1998. *The Planetary Scientist's Companion:* Oxford (Oxford Univ. Press).

McGinnis, C.E., Jain, J.C., and Neal, C.R., 1997. Characterization of memory effects and development of an effective wash protocol for the measurement of petrogenetically critical trace elements in geological samples by ICP-MS. *Geostand. Newsl.,* 21:289–305.

McKenzie, D., and O'Nions, R.K., 1991. Partial melt distributions from inversion of rare earth element concentrations. *J. Petrol.,* 32:1021–1091.

Meschede, M., and Barckhausen, U., 2000. Plate tectonic evolution of the Cocos-Nazca spreading center. *In* Silver, E.A., Kimura, G., Blum, P., and Shipley, T.H. (Eds.), *Proc. ODP, Sci. Results,* 170, 1–10 [Online]. Available from World Wide Web: <**http://www-odp.tamu.edu/publications/170_SR/VOLUME/CHAPTERS/SR170_07.PDF**>.

Meschede, M., and Barckhausen, U., 2001. Plate tectonic evolution of the Cocos-Nazca spreading center. *In* Silver, E.A., Kimura, G., Blum, P., and Shipley, T.H. (Eds.), *Proc. ODP, Sci. Results,* 170, 1–10 [CD-ROM]. Available from: Ocean Drilling Program, Texas A&M University, College Station TX 77845-9547, USA. [**PDF**]

Morris, J.D., Villinger, H.W., Klaus, A., et al., 2003. *Proc. ODP, Init. Repts.,* 205 [CD-ROM]. Available from: Ocean Drilling Program, Texas A&M University, College Station TX 77845-9547, USA. [**HTML**]

Muza, J.P., 2000. Calcareous nannofossil biostratigraphy from a 15-km transect (Cocos plate to Caribbean plate) across the Middle America Trench, Nicoya Peninsula, Costa Rica. *In* Silver, E.A., Kimura, G., Blum, P., and Shipley, T.H. (Eds.), *Proc. ODP, Sci. Results,* 170 [Online]. Available from World Wide Web: <**http://www-odp.tamu.edu/publications/170_SR/chap_05/chap_05.htm**>.

Nui, Y., and Batiza, R., 1997. Trace element evidence from seamounts for recycled oceanic crust in the eastern Pacific mantle. *Earth Planet. Sci. Lett.,* 148:471–483. **doi:10.1016/S0012-821X(97)00048-4**

Nui, Y., Regelous, M., Wednt, I.J., Batiza, R., and O'Hara, M.J., 2002. Geochemistry of near-EPR seamounts: importance of source vs. process and the origin of the enriched mantle component. *Earth Planet. Sci. Lett.,* 199:327–345. **doi:10.1016/S0012-821X(02)00591-5**

Patino, L.C., Carr, M.J., and Feigenson, M.D., 2000. Local and regional variations in Central American arc lavas controlled by variations in subducted sediment input. *Contrib. Mineral. Petrol.,* 138:265–283. **doi:10.1007/s004100050562**

Plank, T., and Langmuir, C.H., 1992. Effects of the melting regime on the composition of the oceanic crust. *J. Geophys. Res.,* 97:19749–19770.

Protti, M., Guendel, F., and McNally, K., 1995. Correlation between the age of the subducted Cocos plate and the geometry of the Wadati-Benioff zone under Nicaragua and Costa Rica. *In* Mann, P. (Ed.), *Geologic and Tectonic Development of the Caribbean Plate Boundary in Southern Central America. Spec. Pap.—Geol. Soc. Am.,* 295.

Ranero, C.R., and von Huene, R., 2000. Subduction erosion along the Middle America convergent margin. *Nature (London, U. K.),* 404:748–752. **doi:10.1038/35008046**

Reynolds, J.R., and Langmuir, C.H., 2000. Identification and implications of off-axis lava flows around the East Pacific Rise. *Geochem., Geophys., Geosyst.,* 1(6). **doi:10.1029/1999GC000033**

Scheirer, D.S., Forsyth, D.W., Cormier, M.-H., and Macdonald, K.C., 1998. Shipboard geophysical indications of asymmetry and melt production beneath the East Pacific Rise near the MELT experiment. *Science,* 280(5367):1221–1224. **doi:10.1126/science.280.5367.1221**

Shipley, T.H., McIntosh, K.D., Silver, E.A., and Stoffa, P.L., 1992. Three-dimensional seismic imaging of the Costa Rica accretionary prism: structural diversity in a small volume of the lower slope. *J. Geophys. Res.,* 97:4439–4459.

Silver, E., Costa Pisani, P., Hutnak, M., Fisher, A., DeShon, H., and Taylor, B., 2004. An 8–10 Ma tectonic event on the Cocos plate offshore Costa Rica: results of Cocos Ridge collision? *Geophys. Res. Lett.,* 31(18). **doi:10.1029/2004GL020272**

Sims, K.W.W., Blichert-Toft, J., Fornari, D.J., Perfit, M.R., Goldstein, S.J., Johnson, P., DePaolo, D.J., Hart, S.R., Murrell, M.T., Michael, P.J., Layne, G.D., and Ball, L.A., 2003. Aberrant youth: chemical and isotopic constraints on the origin of off-axis lavas from the East Pacific Rise, 9°–10°N. *Geochem., Geophys., Geosyst.,* 4(10). **doi:10.1029/2002GC000443**

Sun, S.-S., and McDonough, W.F., 1989. Chemical and isotopic systematics of oceanic basalts: implications for mantle composition and processes. *In* Saunders, A.D., and Norry, M.J. (Eds.), *Magmatism in the Ocean Basins.* Geol. Soc. Spec. Publ., 42:313–345.

Villemant, B., Jaffrezic, H., Joron, J.L. and Treuil, M., 1981. Distribution coefficients of major and trace elements: fractional crystallization in the alkali basalt series of Chaîne des Puys (Massif Central, France). *Geochim. Cosmochim. Acta,* 45(11):1997–2016. **doi:10.1016/0016-7037(81)90055-7**

von Huene, R., Bialas, J., Flueh, E., Cropp, B., Csernok, T., Fabel, E., Hoffmann, J., Emeis, K., Holler, P., Jeschke, G., Leandro, M.C., Perez Fernandez, I., Chavarria, S.J., Florez, H.A., Escobedo, Z.D., Leon, R., and Barrios, L.O., 1995. Morphotectonics of the Pacific convergent margin of Costa Rica. *In* Mann, P. (Ed.), *Geologic and Tectonic Development of the Caribbean Plate Boundary in Southern Central America.* Spec. Pap.—Geol. Soc. Am., 291–307.

von Huene, R., Ranero, C.R., Weinrebe, W., and Hinz, K., 2000. Quaternary convergent margin tectonics of Costa Rica, segmentation of the Cocos plate, and Central American volcanism. *Tectonics,* 19:314–334. **doi:10.1029/1999TC001143**

Werner, R., Hoernle, K., Barckhausen, U., and Hauff, F., 2003. Geodynamic evolution of the Galápagos hot spot system (central East Pacific) over the past 20 m.y.: constraints from morphology, geochemistry, and magnetic anomalies. *Geochem., Geophys., Geosyst.,* 4. **doi:10.1029/2003GC000576**

Werner, R., Hoernle, K., van den Bogaard, P., Ranero, C., von Huene, R., and Korich, D., 1999. Drowned 14-m.y.-old Galápagos archipelago off the coast of Costa Rica: implications for tectonic and evolutionary models. *Geology,* 27(6):499–502. **doi:10.1130/0091-7613(1999)027<0499:DMYOGP>2.3.CO;2**

White, W.M., McBirney, A.R., and Duncan, R.A., 1993. Petrology and geochemistry of the Galápagos Islands: portrait of a pathological mantle plume. *J. Geophys. Res.,* 98:19533–19563.

Wilson, D.S., 1996. Fastest known spreading on the Miocene Cocos–Pacific plate boundary. *Geophys. Res. Lett.,* 23(21):3003–3006. **doi:10.1029/96GL02893**

Wilson, D.S., Teagle, D.A.H., Acton, G.D., et al., 2003. *Proc. ODP, Init. Repts.,* 206 [CD-ROM]. Available from: Ocean Drilling Program, Texas A&M University, College Station TX 77845-9547, USA. [**HTML**]

Workman, R.K., and Hart, S.R., 2005. Major and trace element composition of the depleted MORB mantle (DMM). *Earth Planet. Sci. Lett.,* 231(1–2):53–72. **doi:10.1016/j.epsl.2004.12.005**

Figure F1. Geologic overview of eastern central Pacific seafloor bathymetry and adjacent land elevation, showing locations of ODP Legs 170, 205, and 206, DSDP Hole 504B, the Middle America Trench off Costa Rica, the Cocos-Nazca spreading center, and volcanic products of the Galápagos hotspot, including the Galápagos Islands, the Cocos and Carnegie Ridges, and the Cocos track tholeiites. Also shown is the approximate paleolocation of Subunits 4A and 4B at 14.5 Ma. Convergence direction and rate are from DeMets et al. (1990).

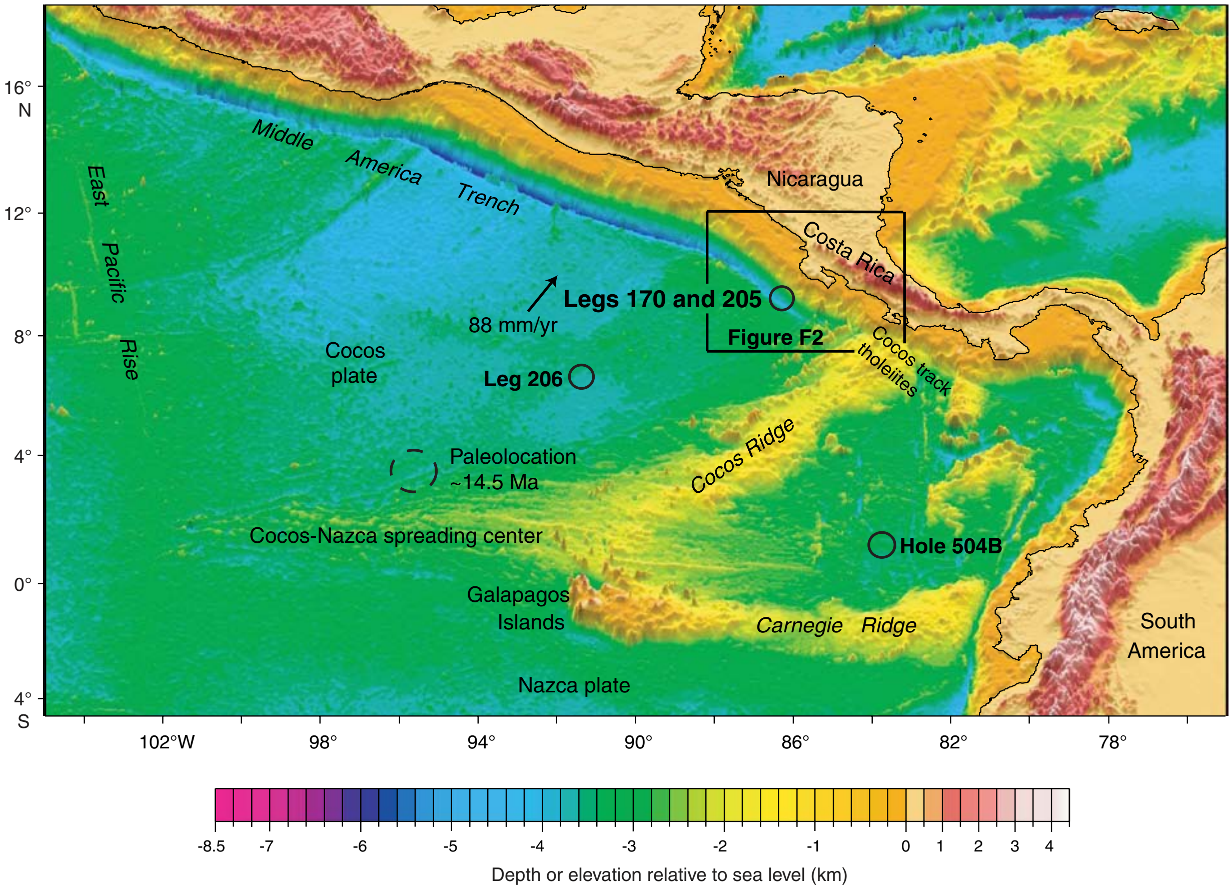

Figure F2. Leg 170 and 205 Costa Rica drilling area and isochrons derived from seafloor magnetic anomalies (Barckhausen et al., 2001). Numbers indicate crustal age in millions of years. Fracture zone trace marks location where spreading of the Cocos-Nazca spreading center (CNS) initiates; triple junction trace separates crust formed at the CNS and the East Pacific Rise. The ridge jump records the change from CNS-1 to CNS-2 spreading (~19.5 Ma). Convergence direction and rate (DeMets et al., 1990) and arc volcanoes (triangles) are also shown. Note the segmentation of the volcanic arc and the offset in Wadati-Benioff Zone isodepths at the Quesada Sharp Contortion (QSC). Figure modified after Barckhausen et al., 2001. Sill intrusion zone redrawn after Silver et al., 2004.

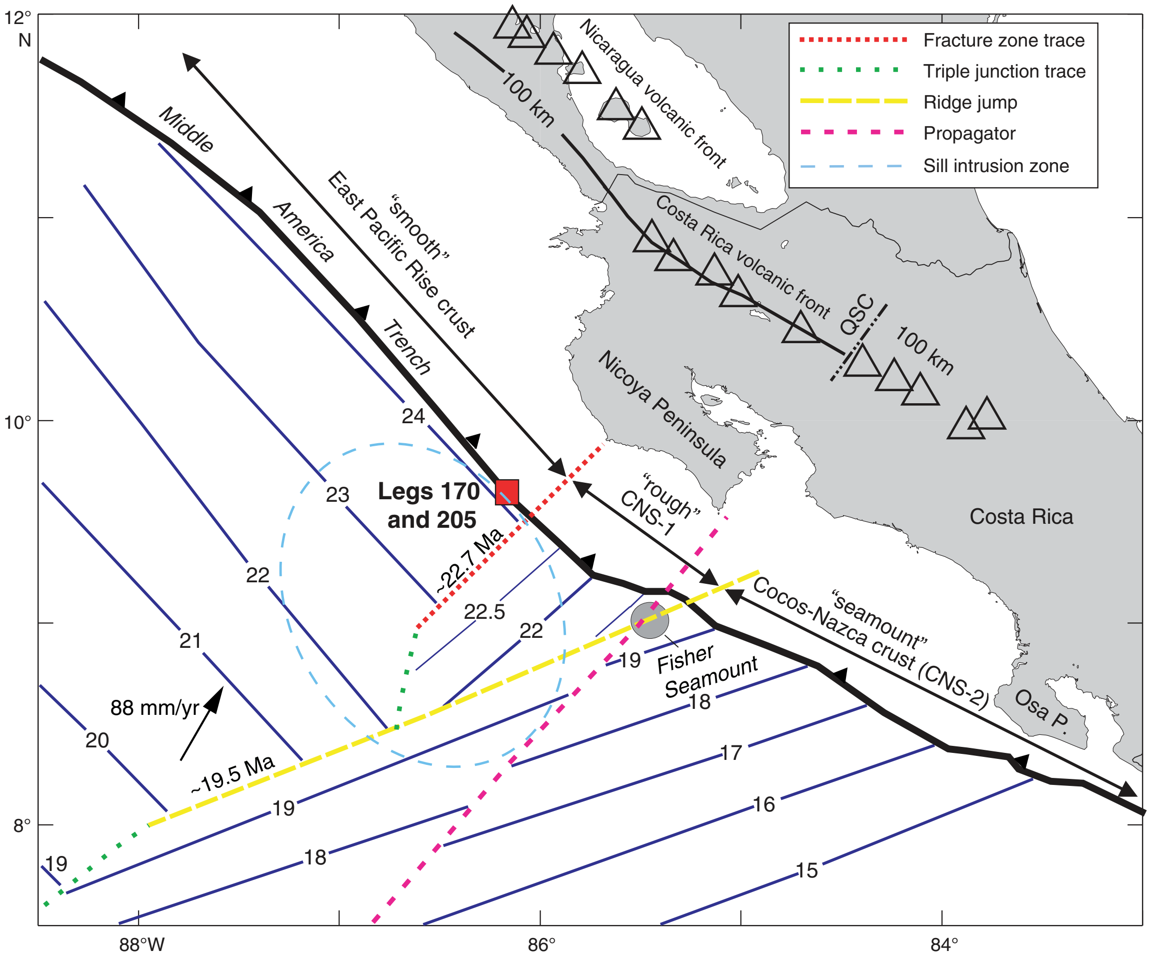

Figure F3. Migrated multichannel seismic profile across the Middle America Trench and location of sedimentary (Units 1–3) and igneous (Subunits 4A and 4B) units cored during Legs 170 and 205 (Morris, Villinger, Klaus, et al., 2003). Note that part of the sequence at Site 1040 is underthrust beneath prism sediments. Unit 1 = diatom ooze with ash, Unit 2 = silty clay with ash-calcareous clay, Unit 3 = siliceous nannofossil-nannofossil chalk with diatoms. P1 = clay with intervals of silt to very fine sand.

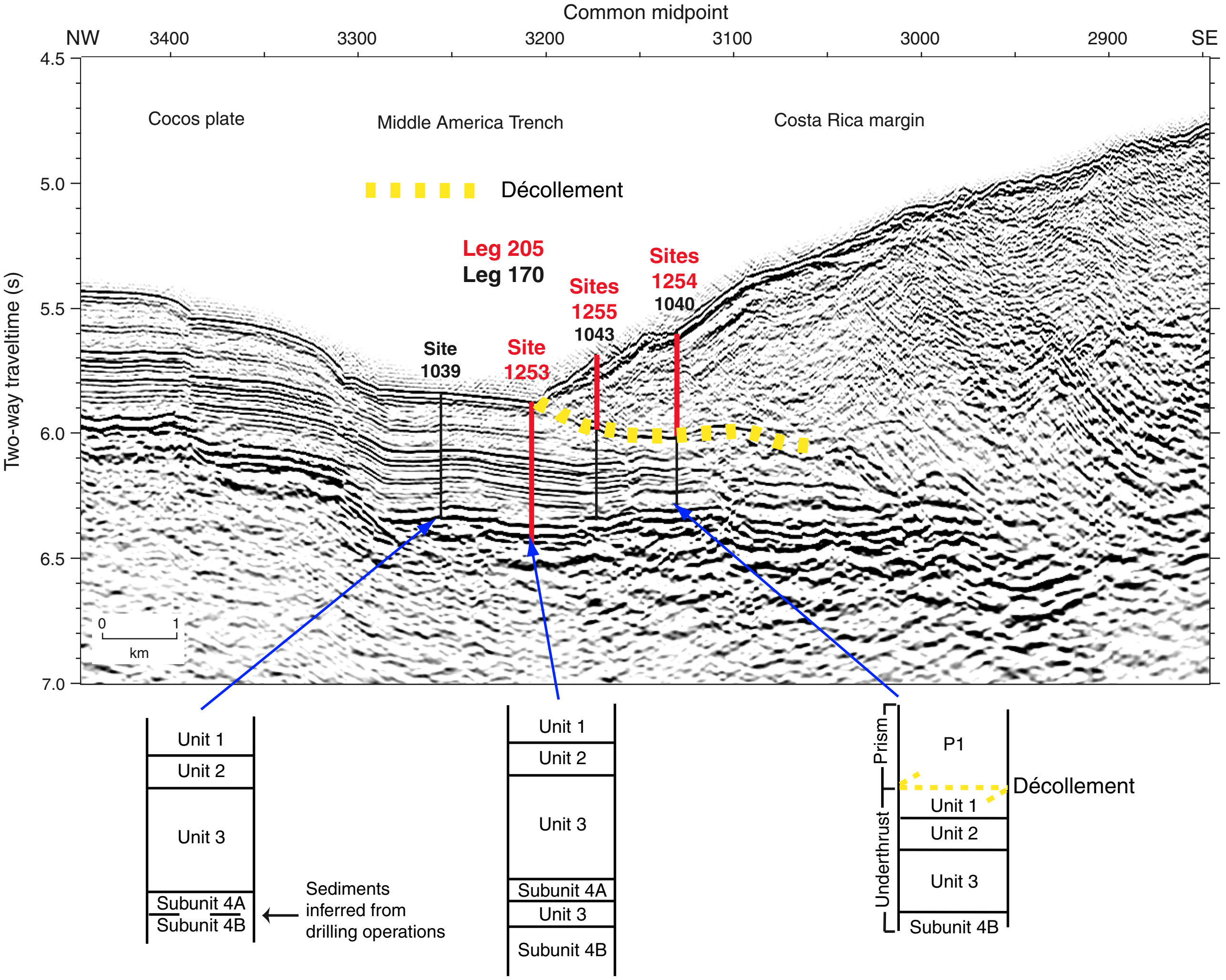

Figure F4. Average core recovery, selected logging data annotated with physical property measurements on cores, and some petrologic observations for units drilled at Site 1253 during Leg 205. Major and minor petrologic boundaries are indicated. Zones labeled 1 to 6 at the base of the lower igneous unit (Subunit 4B) indicate the following observations: 1 = location of basaltic horizon; 2 = greater number of magmatic contacts; 3 = more veins or voids filled with holo- and cryptocrystalline groundmass/altered glass, clay, and zeolites; 4 = up to 5% degree of alteration within 1 m of Section 205-1253A-37R-1 and higher abundance of voids filled with clays and zeolites, ending in an homogeneous microcrystalline gabbro; 5 = increasing number of centimeter-scale fractures and veins; and 6 = homogeneous microcrystalline to fine-grained gabbro with very weak magmatic contacts. Subunit 3C is a calcareous sedimentary horizon. Modified after Morris, Villinger, Klaus, et al., 2003.

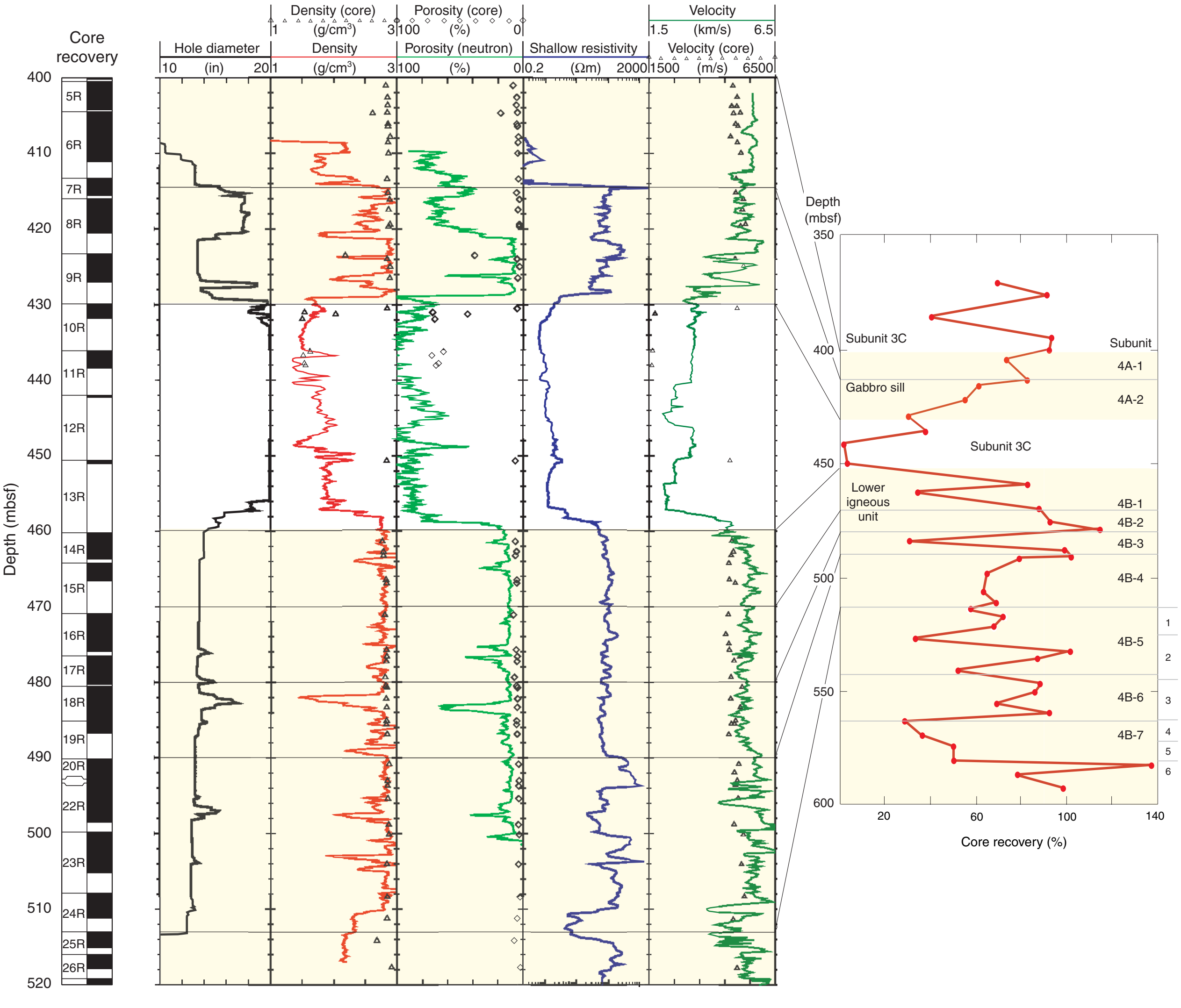

Figure F5. Total alkalis ($Na_2O + K_2O$) vs. SiO_2 for Subunits 4A and 4B of Legs 170 and 205. Includes data from Kimura, Silver, Blum, et al. (1997). All samples are subalkaline. Subunit 4A samples have generally higher total alkali content than the majority of samples from Subunit 4B. Note the relatively restricted range in SiO_2 and the variability of alkalis at a given SiO_2. Also shown are data from Leg 206, the fast-spreading East Pacific Rise deep reference site (Wilson, Teagle, Acton, et al., 2003).

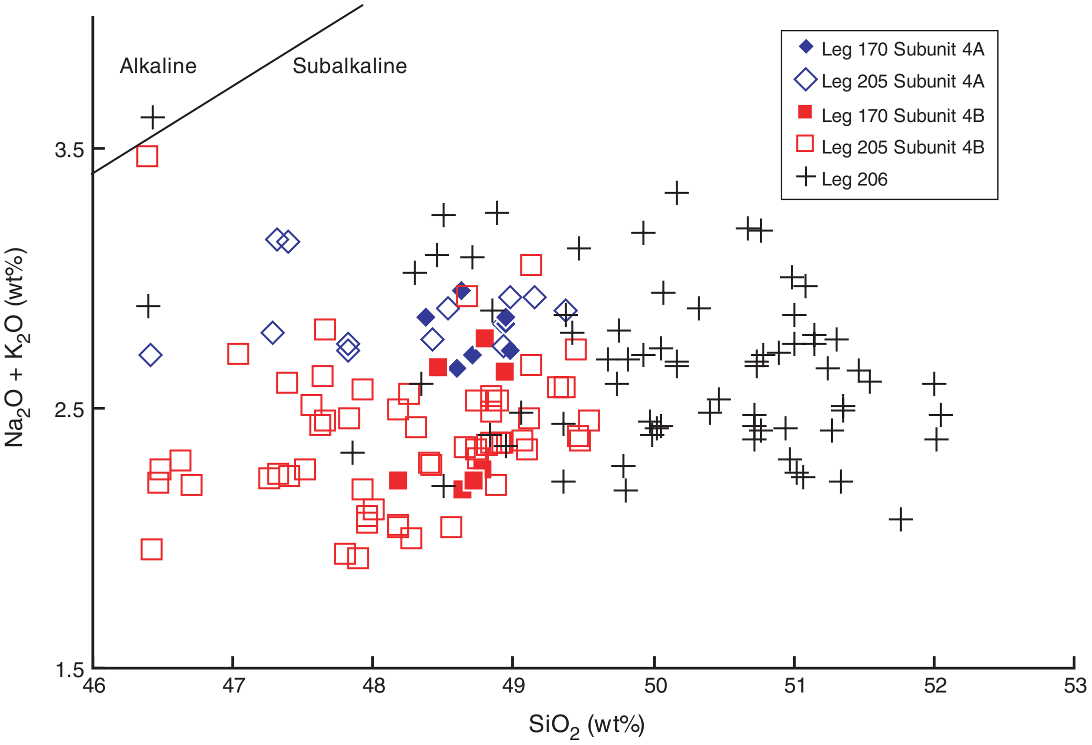

Figure F6. AFM diagram for data from Leg 170 and 205 Subunits 4A and 4B showing the Fe-enrichment trend typical of ocean-floor tholeiites. Subunits 4A and 4B are grouped for clarity. A = $N_2O + K_2O$; F = total Fe as FeO; M = MgO.

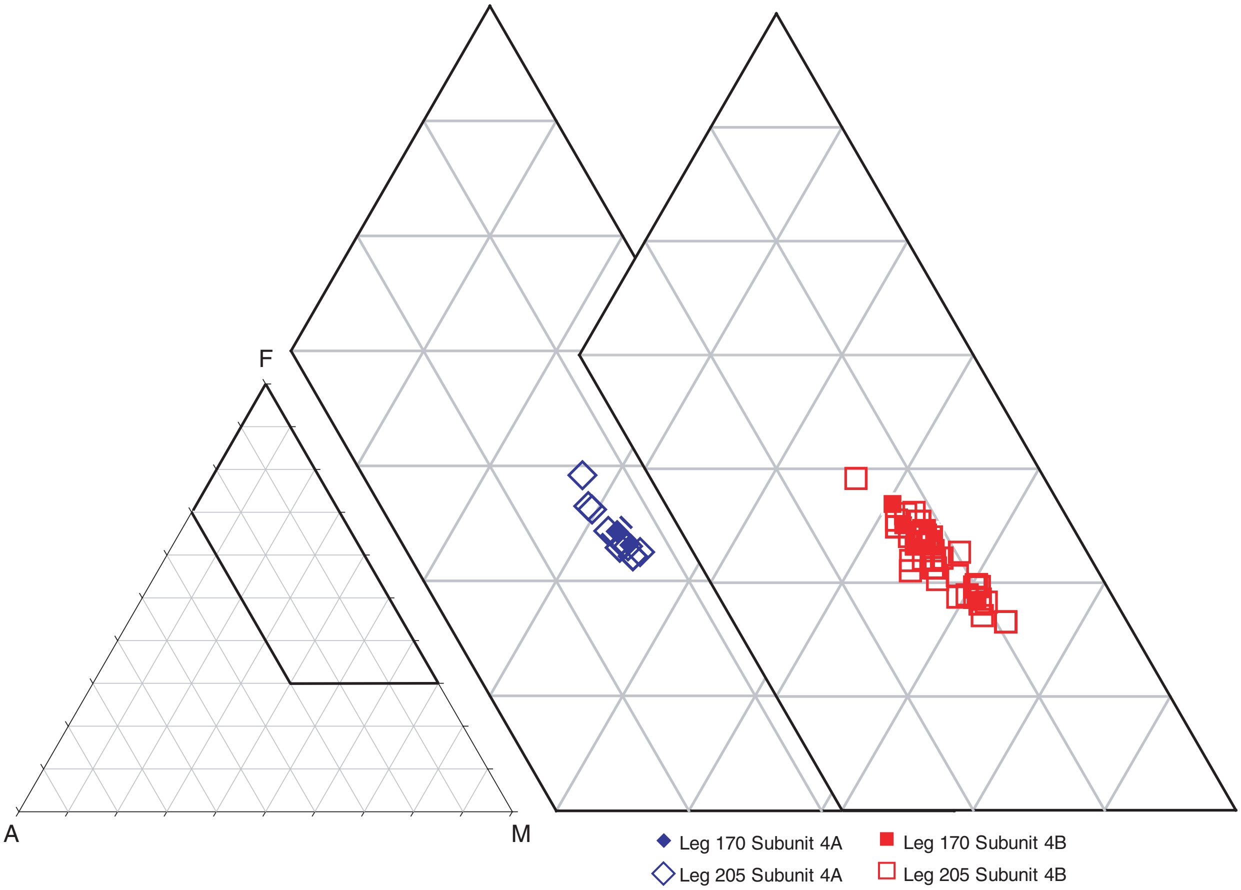

Figure F7. V vs. TiO_2. V and Ti are incompatible in an assemblage of olivine, plagioclase, and clinopyroxene; the positive linear variation of V and TiO_2 reflects their enrichment in the magma during fractional crystallization. The offset trends (Subunit 4A shifts to higher TiO_2) suggest that the units are not derived from a common melting event. The majority of samples from Leg 206 correlate well with the array that includes Subunit 4B. Includes data from Kimura, Silver, Blum, et al. (1997). Also shown are data from Leg 206, the fast-spreading East Pacific Rise deep reference site (Wilson, Teagle, Acton, et al., 2003).

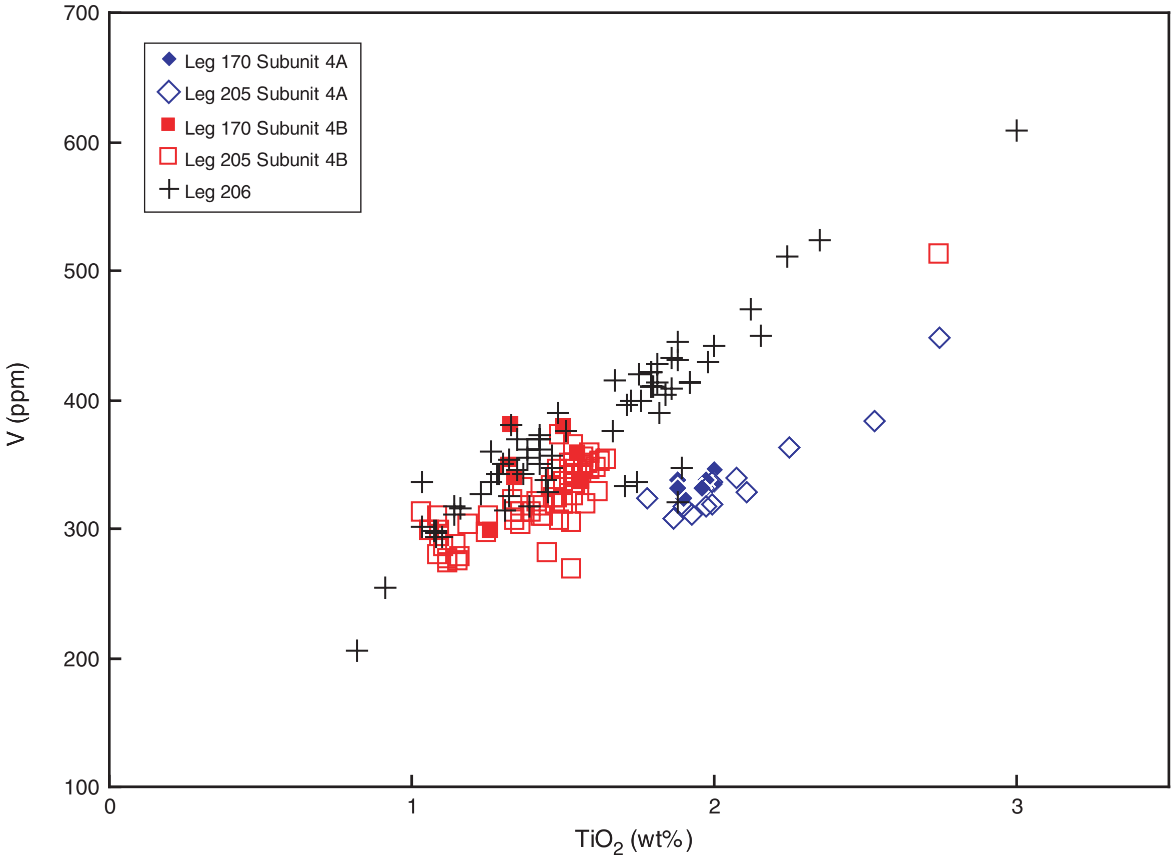

Figure F8. Selected minor and trace element ratios vs. Mg#. Fractionation and alteration processes alone cannot reproduce all of the geochemical variability observed. **A.** K_2O. Alteration and/or differences in partial melting increase alkali variability at given Mg#. **B.** V/TiO_2 is expected to be controlled by original magma composition and proportion of fractionating Fe-Ti and/or clinopyroxene phases. The ratio V/TiO_d is approximately constant over a range of Mg# for Subunit 4A but is more scattered for Subunit 4B, tending to increase with increasing Mg#. These relationships suggest that Subunits 4A and 4B were not generated from a common melting event at a single time. Fractionation is not responsible for the bimodal distribution of (**C**) $(La/Sm)_N$ and (**D**) Hf/Ta ratios. Mg# = [Mg / (Mg + Fe^{+2})]. Includes data from Kimura, Silver, Blum, et al. (1997). Also shown are data from Leg 206, the fast-spreading East Pacific Rise deep reference site (Wilson, Teagle, Acton, et al., 2003). (**Figure shown on next page.**)

Figure F8 (continued). (Caption shown on previous page.)

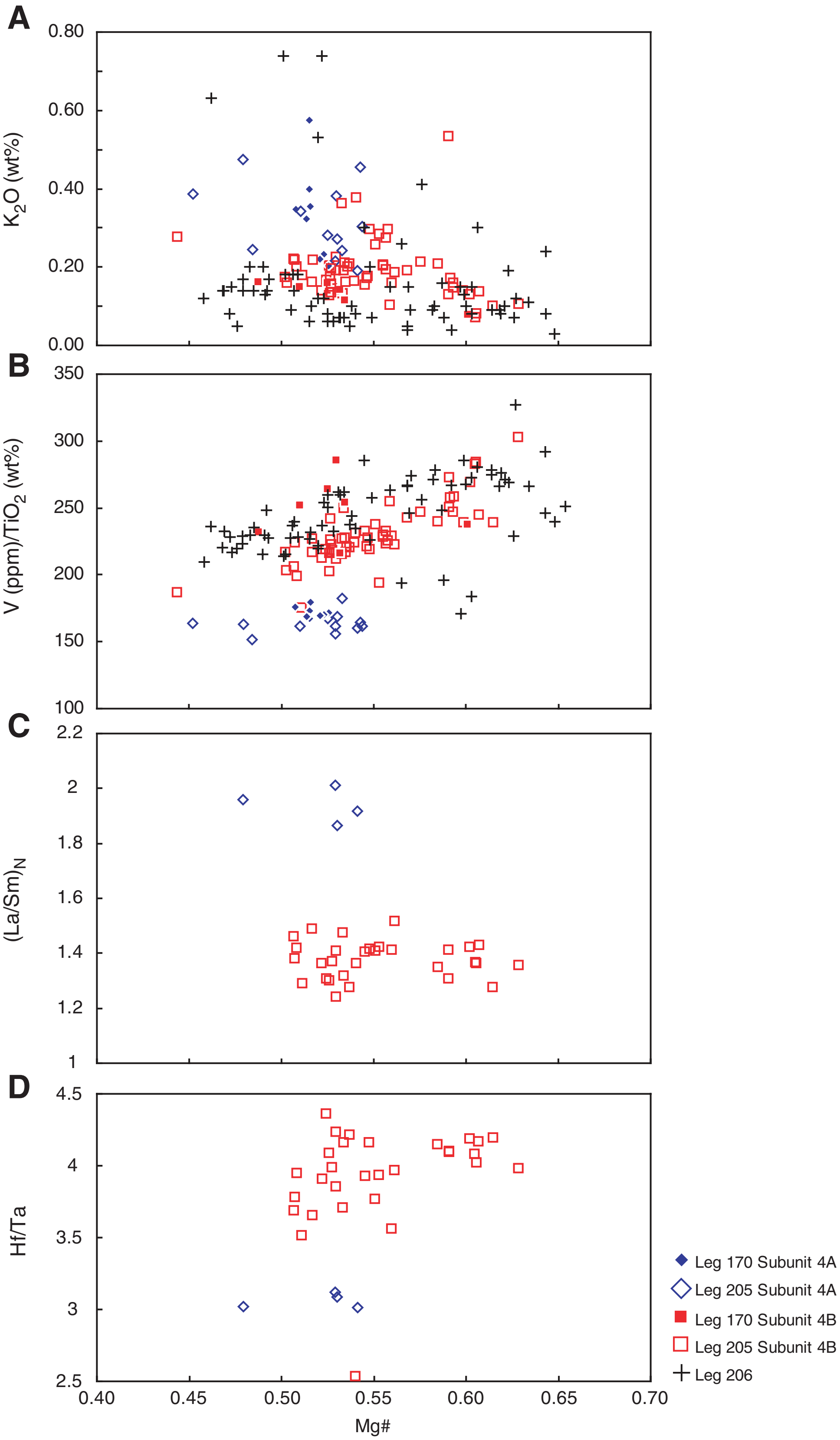

Figure F9. Chondrite-normalized rare earth element (REE) diagram for samples from (**A**) Leg 170 and (**B**) Leg 205 (bottom), along with fields for Galápagos Islands and East Pacific Rise (5°–15°N). Geochemical variability is due to differences in the extent of partial melting and subsequent fractional crystallization and/or crystal accumulation. Note that samples from Leg 170 were measured by INAA, which has poor precision for Nd (see Table T1, p. 33). Normalization values are from Lodders and Fegley, 1998. Includes data from Kimura, Silver, Blum, et al. (1997). Also shown are data from Leg 206, the fast-spreading East Pacific Rise deep reference site (Wilson, Teagle, Acton, et al., 2003).

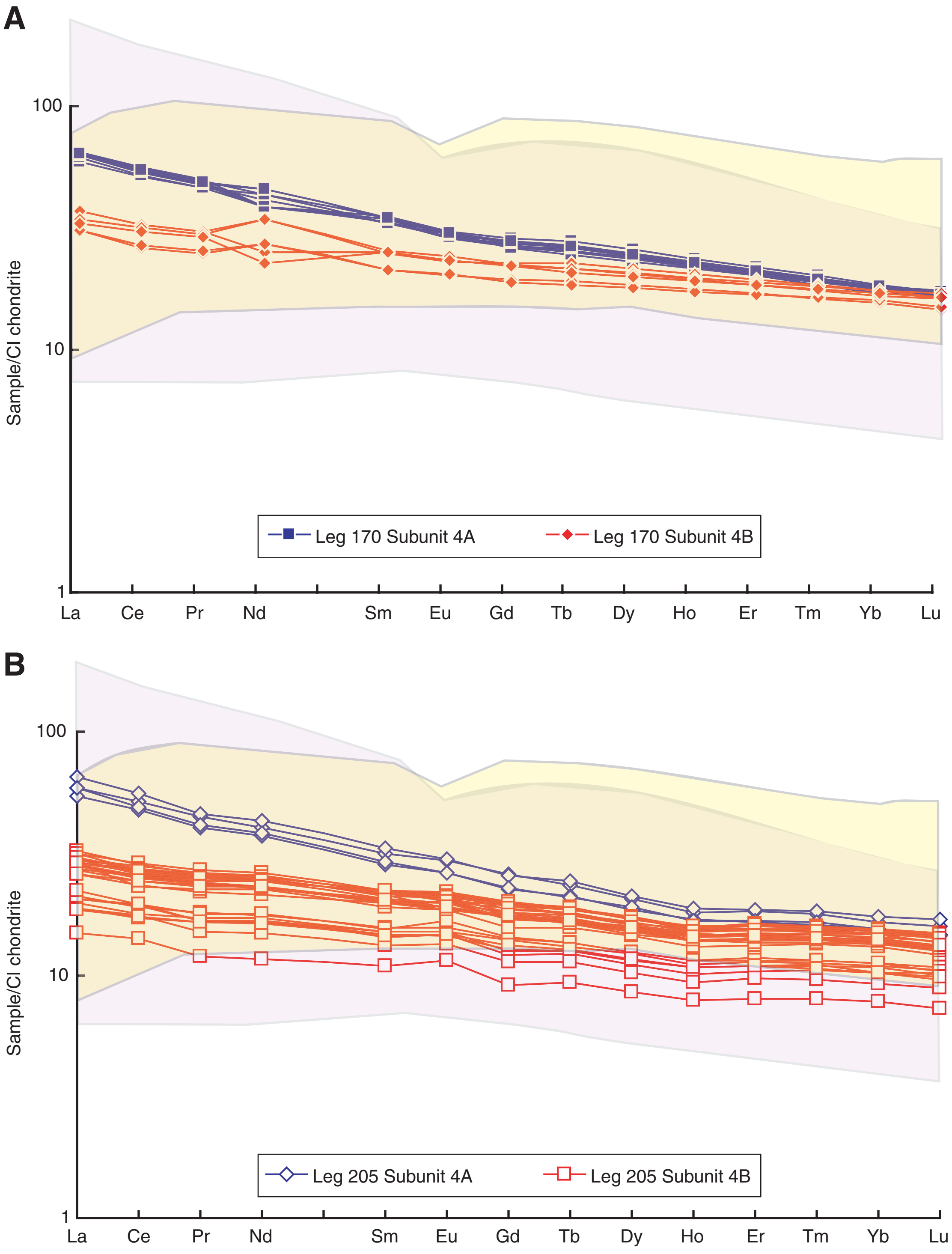

Figure F10. ^{143}Nd/^{144}Nd vs. ^{87}Sr/^{86}Sr, illustrating mixing relationships between regional geochemical end-members. Binary mixing lines are in increments of 10%. Seawater alteration is expected to elevate ^{87}Sr/^{86}Sr, as indicated. The narrow range in Nd isotope values suggests that Subunits 4A and 4B derive from approximately the same source that is a mixture of ~50%–70% enriched (PLUME) and 30%–50% depleted (DMM) sources. The hybrid composition represents mixture of 60% PLUME + 40% DMM end-members. Leg 205 samples do not appear to have a significant admixture of the FLO end-member. East Pacific Rise (EPR; 5°–15°N) and Cocos-Nazca spreading center (CNS) fields are drawn from published data available from the Petrological Database of the Ocean Floor (**www.petdb.org**); Galápagos Island data are from the Geochemistry of Rocks from the Oceans and Continents (GEOROC) database (**georoc.mpch-mainz.gwdg.de/georoc**). Cocos Track tholeiites are selected from analyses by Werner et al. (2003) and Harpp et al. (2005). PLUME, DMM, and FLO represent regional geochemical end-members after (Harpp and White, 2001). Leg 205 data are from V. Chavagnac, unpubl. data. Model input parameters as follows: PLUME: ^{87}Sr/^{86}Sr = 0.70331, ^{143}Nd/^{144}Nd = 0.512887, Sr = 21.1 ppm, and Nd = 1.354 ppm; FLO: 0.7045, 0.51283, 45, and 2; DMM: 0.702389, 0.513181, 7.664, and 0.581; hybrid: 70313, 0.51295, 15.726, and 1.045. PLUME concentration data from Sun and McDonough, 1989. PLUME and DMM isotope values from analyses of published values for EPR and the Galápagos Islands. FLO isotope data from Harpp and White, 2001. FLO concentration data are estimated from reasonable back-calculation of lavas from Isla Floreana (White et al., 1993). DMM concentration data are from Workman and Hart (2005).

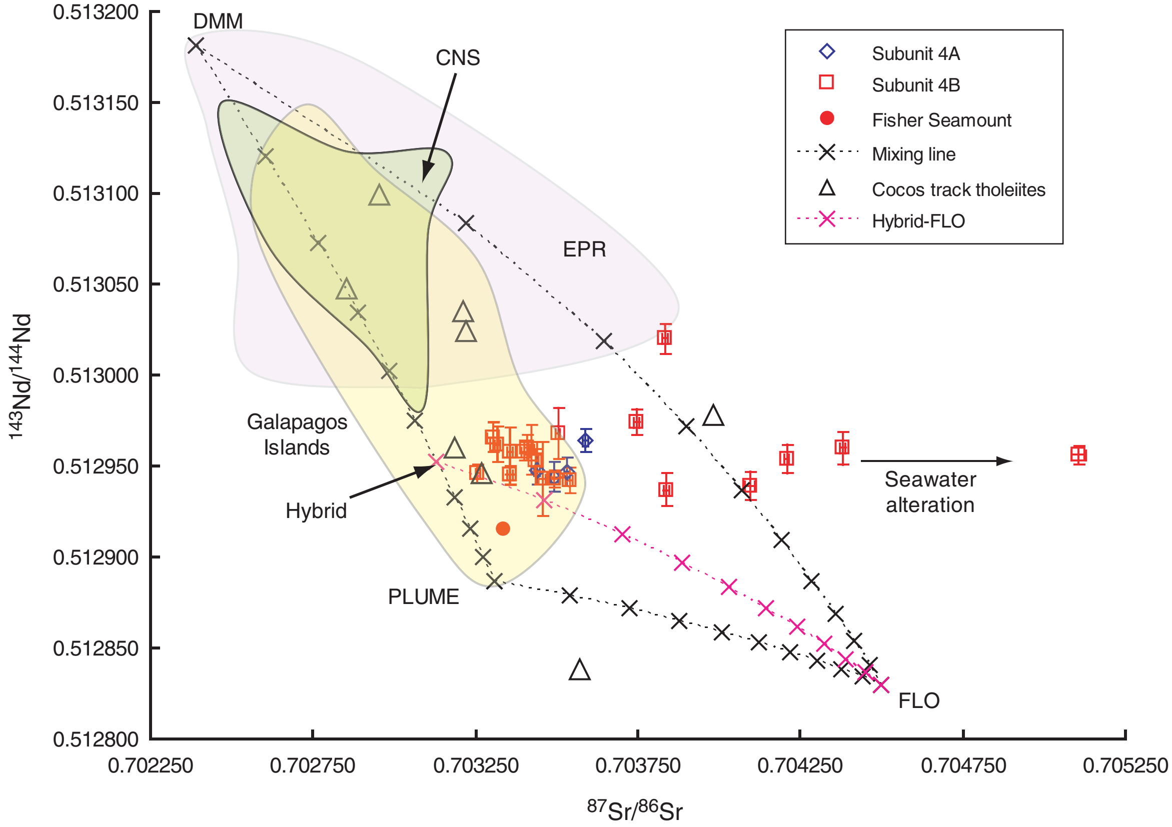

Figure F11. A. $(La/Sm)_N$ vs. Hf/Ta for Subunits 4A and 4B. Also shown are East Pacific Rise (EPR) basaltic glasses (5°–15°N) and Cocos-Nazca spreading center (CNS) and Galápagos Islands basalts extracted from published geochemical data (GEOROC and PetDB Web sites). Samples from the CNS and EPR generally have Hf/Ta >10 with $(La/Sm)_N$ ~0.5–1. Galápagos Island data have Hf/Ta <5, as do Subunits 4A and 4B, with $(La/Sm)_N$ = ~1–2.5. The highest $(La/Sm)_N$ values of the Galápagos Islands are from the anomalous "main series" of Isla Floreana, thought to be related to partial melting of an ITE-rich source distinct from the other islands in the Galápagos (Bow and Geist, 1992; Harpp and White, 2001). Averages of oceanic island basalt (OIB), mid-ocean-ridge basalt (MORB), and primitive mantle (PM) are from Sun and McDonough (1989). Includes data from Kimura, Silver, Blum, et al. (1997). Also shown are data from Leg 206, the fast-spreading East Pacific Rise deep reference site (Wilson, Teagle, Acton, et al., 2003). For clarity, Cocos track tholeiites are not shown. (Continued on next page.)

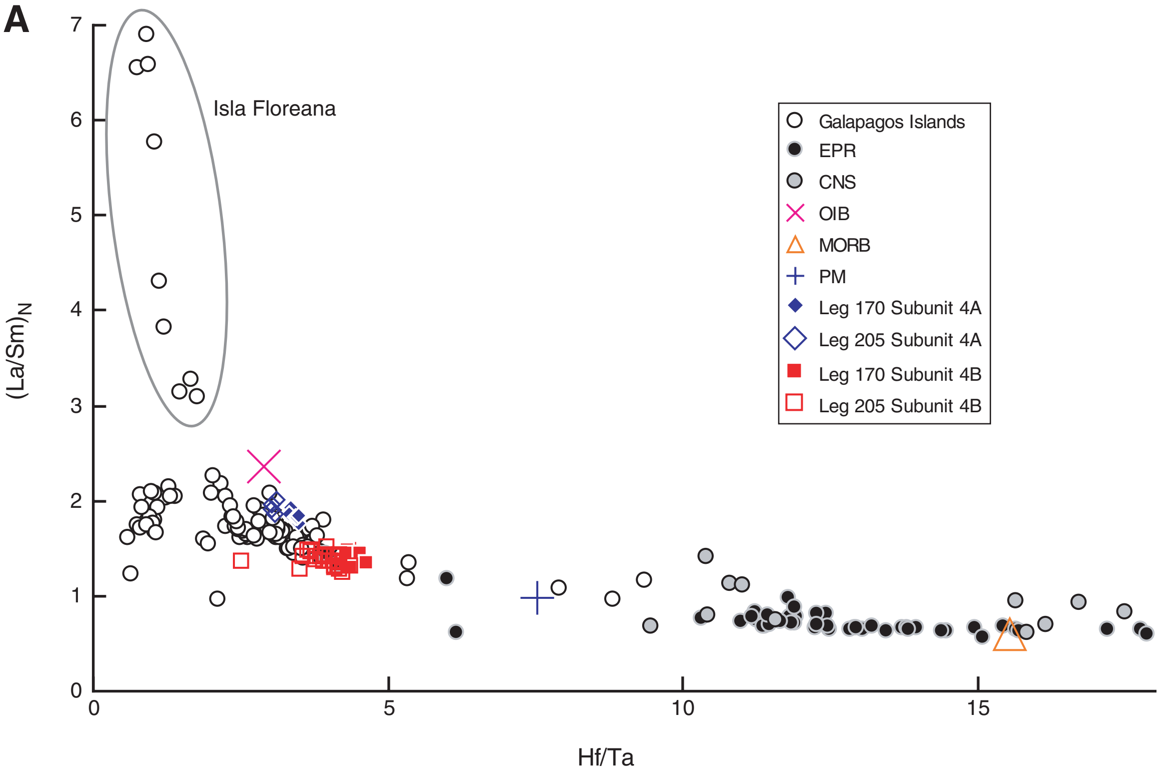

Figure F11 (continued). B. $(La/Sm)_N$ vs. Hf/Ta illustrating the relative importance of binary mixing, partial melting, and fractional crystallization. Batch melting trajectories are shown for a hybrid composition that is 60% enriched. Numbers next to partial melting curves represent percentage of partial melt. The *pathway* differences in marking the garnet and spinel fields are negligible, but the degrees of melting vary slightly along a given path. Inset shows the effect of 50% fractional crystallization that is minor and has a trend distinct from that of partial melting. Liquid lines of descent trend towards lower $(La/Sm)_N$ and Hf/Ta because of the lower bulk incompatibilities of La and Hf compared to Sm and Ta, respectively. Includes data from Kimura, Silver, Blum, et al. (1997). Also shown are data from Leg 206, the fast-spreading East Pacific Rise deep reference site (Wilson, Teagle, Acton, et al., 2003). Batch melting modes of peridotite following Kinzler (1997): olivine = 53%, orthopyroxene = 27%, clinopyroxene = 17%, and Al-phase (garnet or spinel) = 3%: $C_L = C_O/[D + F(1 - D)]$, where C_L is the concentration of the liquid, C_O is the concentration of the original solid, F is the fraction of melt produced, and D is the bulk distribution coefficient of the original solid. Fractional crystallization modes approximate volume percent phenocrysts in samples (Kimura, Silver, Blum et al., 1997): $C_L = C_O F^{(D-1)}$, where C_L is concentration residual liquid and F is the fraction of melt remaining. Partition coefficient data from McKenzie and O'Nions (1991) except plagioclase-Hf from Villemant et al. (1981).

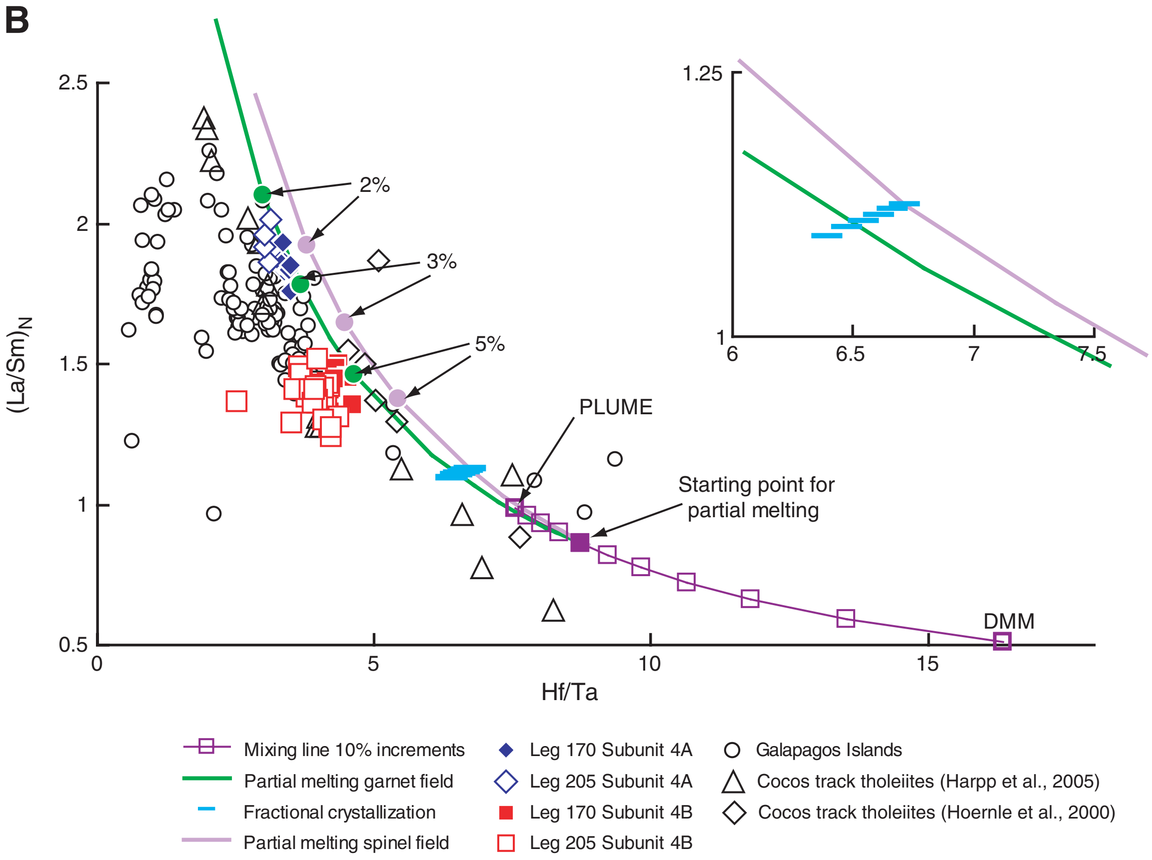

Figure F12. Crystal accumulation model for the rare earth element (REE) range observed in Subunit 4B. In this model an instantaneous solid crystallized from the most enriched Subunit 4B sample is incrementally added to the most enriched sample composition for Subunit 4B until a match is found for the least enriched composition of Subunit 4B. The composition of the instantaneous solid is constrained by the modal abundances observed in Leg 170 samples (Kimura, Silver, Blum, et al., 1997) and the partition coefficient data of McKenzie and O'Nions (1991) (olivine, orthopyroxene, clinopyroxene, and plagioclase) and Agee (1990) (magnetite). We assume that the instantaneous solid is a product of fractional crystallization from liquids with the composition of the more enriched samples from Subunit 4B. Mineral compositional data are required to confirm this assumption; therefore, more quantitative modeling is deferred. The difference between the lowest REE abundance sample in Subunit 4B and the model result is also shown. As modeled, crystal accumulation does not appreciably alter the slope of the REE and reproduces the slight positive Eu anomaly observed in the lowest abundance samples from Subunit 4B. Note that the highest REE abundance within Subunit 4B occurs from Leg 170, but this model uses the highest Subunit 4B sample from Leg 205 to avoid potential laboratory bias and because of the generally improved precision of ICP-MS analyses. Normalization values are from Lodders and Fegley, 1998.

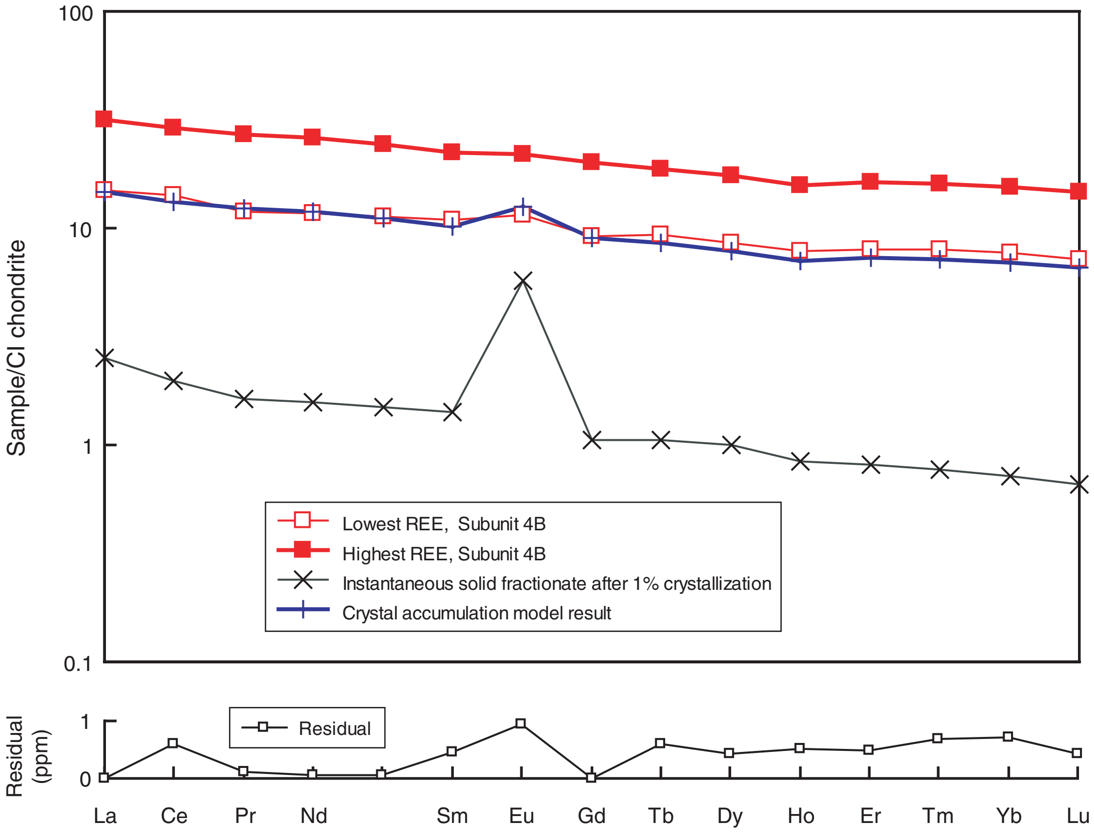

Table T1. Analysis of standard reference materials. (Continued on next page.)

	XRF						INAA				
Element oxide (wt%)	BIR-1			BHVO-2				JGb-1			
	Measured	Certified	±	Measured	Certified	±	Element	Mean	Certified	±	Guevara et al., 2001
SiO_2	47.668	47.96	0.19	49.708	49.9	0.6	FeO_T (wt%)	13.64	13.55		13.33
TiO_2	0.95	0.96	0.01	2.77	2.73	0.04	CaO (wt%)	12.56	11.90		11.90
Al_2O_3	15.42	15.5	0.15	13.58	13.5	0.2	Na_2O (wt%)	1.23	1.20		1.21
Fe_2O_{3T}	11.57	11.3	0.12	12.47	12.3	0.2	Zr (ppm)	20	32.8	6.8	32
MnO	0.183	0.175	0.003	0.175	0.100	0.003	Sr (ppm)	348	327	39	327
MgO	9.61	9.70	0.079	7.34	7.23	0.12	Cr (ppm)	57	57.8	13.5	59
CaO	13.23	13.3	0.12	11.31	11.4	0.2	Ba (ppm)	64	64.3	17.1	62
Na_2O	1.80	1.82	0.045	2.34	2.22	0.08	Sc (ppm)	34.7	35.8	2.1	35.9
K_2O	0.02	0.030	0.003	0.51	0.52	0.01	Co (ppm)	61.1	60.1	5.8	61.1
P_2O_5	0.05	0.021	0.001	0.26	0.27	0.02	La (ppm)	3.47	3.60	0.56	3.57
LOI	–0.49			–0.5			Ce (ppm)	8.1	8.17	1.00	8.1
Total	100.00			99.96			Nd (ppm)	4.3	5.47	0.83	5.3
							Sm (ppm)	1.42	1.49	0.19	1.49
							Eu (ppm)	0.61	0.62	0.052	0.606
							Tb (ppm)	0.27	0.29	0.071	0.268
							Yb (ppm)	0.92	1.06	0.071	0.93
							Lu (ppm)	0.142	0.15	0.025	0.147
							Hf (ppm)	0.84	0.88	0.19	0.823
							Ta (ppm)	0.15	0.18	0.076	0.133
							Th (ppm)	0.42	0.48	0.10	0.43
							U (ppm)	0.06	0.13	0.048	0.115

Note: RSD = relative standard deviation.

Table T1 (continued).

	ICP-MS									
	BIR-1					JGb-1				
Element (ppm)	Mean	RSD (%)	Certified	±	Eggins et al., 1997	Mean	RSD (%)	Certified	±	Guevara et al., 2001
Li	3.5	8.8	3.6	0.2	3.32	5.1	6.7	4.59	0.90	4.59
Be	0.08	16.0	0.58		0.116	0.30	8.0	0.34	0.014	0.34
Rb	0.3	5.5			0.195	6.0	7.2	6.87	3.00	5.5
Sb	0.414	6.1	0.58		0.5	0.092	8.7	0.085	0.048	0.1
Cs	0.009	50.1			0.0053	0.225	2.3	0.26	0.076	0.218
Pb	2.78	16.7	3		2.97	1.39	16.8	1.92	0.74	1.62
Sc	44.7	2.0	44	1	43.8	34.8	3.1	35.8	2.1	35.9
V	337.1	5.8	310	11	322	690.1	1.6	635	58	650
Cr	408.6	2.8	370	8	412	58.4	3.3	57.8	13.5	59
Co	55.6	2.8	52	2	53	64.2	3.6	60.1	5.8	61.1
Ni	177.4	4.7	170	6	175	35.9	1.7	25.4	5.7	24
Cu	121.6	4.0	125	4	113	84.7	1.4	85.7	5.6	86.3
Zn	79.4	3.2	70	9	65	119.5	6.8	109	8.0	109
Ga	16.3	1.1	16		15.2	19.6	2.7	17.9	3.3	17.9
Sr	114.8	2.2	110	2	106.4	332.1	0.8	327	39	327
Y	14.1	5.1	16	1	16.20	8.5	4.7	10.4	2.4	10.1
Ba	7.63	31.9	7		6.52	62.1	3.7	64.3	17.1	62
La	0.58	3.2	0.63	0.07	0.604	3.38	1.6	3.60	0.56	3.57
Ce	1.82	4.9	1.9	0.4	1.897	8.15	3.5	8.17	1.00	8.1
Pr	0.35	2.9			0.378	1.09	2.8	1.13	0.14	1.128
Nd	2.30	3.3	2.5	0.7	2.38	5.06	2.7	5.47	0.83	5.3
Sm	1.05	3.0	1.1		1.117	1.40	1.9	1.49	0.19	1.49
Eu	0.52	2.7	0.55	0.05	0.524	0.61	2.8	0.62	0.052	0.606
Gd	1.70	11.3	1.8	0.4	1.850	1.55	4.2	1.61	0.14	1.6
Tb	0.35	5.7			0.379	0.27	3.9	0.29	0.071	0.268
Dy	2.37	3.2	4	1	2.53	1.65	3.1	1.56	0.37	1.61
Ho	0.53	4.1			0.585	0.34	4.4	0.33	0.052	0.34
Er	1.58	3.2			1.734	0.96	3.1	1.04	0.24	1.01
Tm	0.25	4.1				0.15	3.0	0.16	0.033	0.155
Yb	1.59	2.5	1.7	0.1	1.649	0.91	1.7	1.06	0.30	0.93
Lu	0.24	1.7	0.26		0.247	0.13	1.8	0.15	0.025	0.147
Zr	15.9	7.0	18	1	14.47	28.4	4.0	32.8	6.8	32
Nb	0.69	8.0	0.6		0.558	2.3	7.8	3.34	1.33	2.6
Hf	0.57	3.1	0.6	0.08	0.562	0.8	3.5	0.88	0.19	0.823
Ta	0.052	19.6			0.041	0.17	12.1	0.18	0.076	0.133
Th	0.028	21.8			0.0302	0.43	8.0	0.48	0.10	0.43
U	0.01	20.1			.0100	0.10	1.7	0.13	0.048	0.115

Table T2. XRF and ICP-MS analysis of Subunits 4A and 4B, Hole 1253A. (Continued on next two pages.)

Core, section:	4R-CC	7R-2	8R-2	10R-1	12R-1	13R-1	14R-1	15R-1	16R-2	17R-2	18R-1	18R-4	21R-1
Interval (cm):	21–22	71–75	82–87	68–71	29–34	38–42	17–22	39–45	36–41	34–38	81–85	77–80	47–49
Unit:	4A-1	4A-1	4A-2	4A-2	4B-1	4B-1	4B-1	4B-1	4B-2	4B-2	4B-3	4B-3	4B-4
Depth (mbsf):	400.16	415.48	418.2	430.58	442.29	450.98	460.37	464.59	472.76	477.44	481.31	484.9	493.27
Major element oxide (wt%):													
SiO_2	48.54	48.93	48.98	49.37	48.74	49.45	48.18	48.89	48.01	48.28	49.14	48.18	47.81
TiO_2	1.992	1.990	2.075	1.971	1.569	1.480	1.090	1.151	1.089	1.146	1.491	1.159	1.031
Al_2O_3	14.68	14.34	16.04	14.46	15.58	16.55	15.67	16.14	16.02	15.50	13.95	15.87	14.98
Fe_2O_{3T}	12.53	12.26	12.80	12.26	12.10	10.81	10.86	10.71	10.79	11.18	13.33	11.17	10.83
FeOT	11.28	11.03	11.51	11.04	10.88	9.73	9.77	9.64	9.71	10.06	11.99	10.05	9.74
MnO	0.181	0.198	0.186	0.181	0.216	0.190	0.177	0.176	0.160	0.172	0.188	0.170	0.189
MgO	7.14	7.30	5.95	6.96	6.97	6.61	8.30	8.62	8.36	8.15	7.71	7.94	9.25
CaO	11.52	11.39	10.44	11.70	12.44	12.44	12.30	12.55	12.20	12.51	11.31	12.51	12.56
Na_2O	2.62	2.54	2.45	2.66	2.39	2.42	1.92	2.10	2.02	1.86	2.47	1.83	1.83
K_2O	0.27	0.19	0.48	0.21	0.13	0.30	0.13	0.10	0.08	0.13	0.19	0.21	0.10
P_2O_5	0.223	0.238	0.249	0.247	0.149	0.116	0.097	0.107	0.090	0.093	0.135	0.111	0.082
LOI	0.30	0.48	0.55	0.04	0.03	–0.07	1.00	–0.04	1.10	1.02	0.52	0.91	1.14
Total	99.99	99.86	100.18	100.08	100.31	100.29	99.73	100.51	99.92	100.05	100.44	100.05	99.80
Mg#	0.53	0.54	0.48	0.53	0.53	0.55	0.60	0.61	0.61	0.59	0.53	0.58	0.63
Trace element (ppm):													
Li	3.9	4.4	6.7	3.9	2.6	1.9	3.8	5.8	5.3	4.4	4.4	5.1	3.7
Be	0.74	0.62	0.81	0.62	0.49	0.41	0.28	0.30	0.32	0.31	0.42	0.33	0.46
Rb	6.21	2.39	8.40	2.99	1.19	1.50	2.21	1.02	1.02	1.82	3.25	4.24	3.01
Sb	0.072	0.040	0.040	0.083	0.118	0.380	0.038	0.048	0.036	0.047	0.042	0.048	0.049
Cs	0.172	0.022	0.039	0.046	0.013	0.002	0.044	0.012	0.012	0.024	0.018	0.062	0.047
Pb	0.28	0.20	0.48	0.39	0.28	0.53	0.56	0.09	0.14	0.28	0.78	0.35	0.24
Sc	41.4	41.4	34.6	44.4	42.7	43.7	47.4	41.7	40.0	44.0	46.7	39.1	41.0
V	336.1	319.3	338.8	317.9	355.7	323.7	293.6	275.2	309.3	286.9	372.7	277.8	311.9
Cr	268.7	256.5	92.8	256.8	193.1	284.0	426.9	353.7	341.9	391.4	68.1	300.4	205.7
Co	48.0	45.1	44.6	43.4	47.7	45.2	46.5	47.2	48.4	46.3	49.4	45.3	46.4
Ni	87.6	92.8	64.7	96.0	95.4	109.1	143.2	132.6	145.1	136.8	71.2	116.0	86.9
Cu	127.1	68.6	170.9	140.1	148.1	148.0	144.1	79.2	145.0	166.3	187.6	133.2	164.5
Zn	127.8	68.8	137.8	81.5	109.8	80.6	87.9	55.6	79.1	71.6	121.4	71.2	80.9
Ga	19.2	17.9	20.3	17.5	18.8	17.0	17.7	15.3	16.6	16.3	18.1	16.0	17.8
Sr	227.4	223.7	227.6	236.2	205.3	222.9	164.3	157.6	152.3	154.0	167.3	143.4	172.2
Y	26.9	26.7	26.9	26.7	22.6	23.9	17.2	17.3	16.0	17.0	23.4	17.7	22.9
Ba	80.2	74.3	107.5	81.7	128.8	93.9	59.9	40.8	35.2	40.4	53.6	39.0	53.3
La	13.86	12.83	15.27	13.87	7.64	6.80	4.80	4.39	4.81	4.62	6.11	4.96	7.02
Ce	32.11	29.56	34.37	30.34	17.52	16.84	12.12	10.63	12.01	10.98	14.49	11.75	17.42
Pr	4.22	3.80	4.32	3.90	2.45	2.21	1.57	1.55	1.57	1.61	2.05	1.70	2.45
Nd	18.46	17.05	19.78	17.61	11.76	10.46	7.70	7.59	7.64	7.86	9.86	8.11	11.71
Sm	4.75	4.27	4.98	4.40	3.31	3.07	2.16	2.20	2.25	2.26	2.96	2.35	3.30
Eu	1.68	1.50	1.72	1.51	1.23	1.12	0.84	0.82	0.86	0.86	1.14	0.89	1.21
Gd	5.20	4.51	5.10	4.59	3.72	3.42	2.43	2.55	2.50	2.77	3.43	2.82	3.83
Tb	0.87	0.78	0.90	0.77	0.66	0.61	0.45	0.46	0.46	0.48	0.62	0.50	0.68
Dy	5.12	4.60	5.30	4.75	4.07	3.89	2.75	2.91	2.88	3.04	3.94	3.10	4.26
Ho	1.02	0.94	1.04	0.94	0.86	0.78	0.57	0.60	0.60	0.62	0.81	0.64	0.86
Er	2.92	2.64	2.98	2.67	2.48	2.24	1.66	1.74	1.73	1.82	2.33	1.87	2.48
Tm	0.45	0.40	0.46	0.41	0.38	0.36	0.26	0.27	0.27	0.28	0.37	0.29	0.38
Yb	2.65	2.47	2.78	2.49	2.45	2.23	1.62	1.64	1.72	1.73	2.25	1.79	2.35
Lu	0.40	0.36	0.42	0.36	0.35	0.33	0.24	0.25	0.25	0.26	0.33	0.27	0.36
Zr	161.3	197.8	169.3	157.4	102.9	136.0	69.0	63.6	67.5	68.3	78.9	72.4	91.8
Nb	20.7	19.6	21.8	18.1	11.0	9.1	6.7	6.1	7.4	6.9	8.2	7.0	10.6
Hf	3.68	3.49	3.83	3.64	2.42	2.43	1.68	1.63	1.65	1.71	1.97	1.78	2.46
Ta	1.19	1.16	1.27	1.17	0.65	0.58	0.40	0.39	0.41	0.42	0.47	0.43	0.62
Th	1.85	1.72	1.84	1.78	0.97	0.84	0.61	0.56	0.60	0.52	0.67	0.59	0.90
U	0.70	0.50	0.52	0.50	0.29	0.33	0.17	0.14	0.16	0.16	0.19	0.16	0.25

Table T2 (continued).

Core, section:	22R-5	23R-3	24R-2	25R-1	25R-1	26R-2	27R-2	28R-1	23R-2	30R-2	31R-1	32R-3	34R-1
Interval (cm):	106–109	96–100	36–39	30–34	80–84	22–25	64–68	31–36	28–33	22–26	30–34	40–44	42–46
Unit:	4B-4	4B-4	4B-4	4B-5	4B-5	4B-5	4B-5	4B-5	4B-5	4B-5	4B-5	4B-6	4B-6
Depth (mbsf):	499.31	503.53	509.72	513.3	513.8	517.66	520.96	524.21	530.38	536.22	538.8	546.15	553.32
Major element oxide (wt%):													
SiO_2	47.90	47.96	47.84	48.19	48.26	48.74	48.86	48.93	48.75	49.38	49.10	48.91	48.57
TiO_2	1.057	1.119	1.094	1.450	1.536	1.525	1.531	1.587	1.488	1.504	1.531	1.361	1.341
Al_2O_3	15.66	15.14	15.78	15.90	15.56	15.38	15.71	15.09	15.52	15.87	15.77	15.21	14.50
Fe_2O_{3T}	10.73	11.33	11.24	12.00	12.21	12.58	12.13	12.31	12.57	11.77	12.11	11.83	12.26
FeOT	9.65	10.20	10.12	10.80	10.99	11.32	10.92	11.08	11.31	10.59	10.90	10.64	11.03
MnO	0.170	0.175	0.163	0.209	0.222	0.198	0.189	0.188	0.191	0.177	0.176	0.194	0.187
MgO	8.30	8.84	8.19	7.50	7.56	6.79	6.41	6.94	6.53	6.12	6.33	7.64	7.88
CaO	12.96	11.84	11.85	11.86	11.67	12.36	12.56	11.87	12.28	12.43	12.44	12.47	12.69
Na_2O	1.85	1.95	1.92	2.21	2.29	2.17	2.36	2.22	2.08	2.36	2.14	2.17	1.88
K_2O	0.07	0.14	0.53	0.28	0.26	0.16	0.18	0.14	0.22	0.22	0.20	0.19	0.16
P_2O_5	0.088	0.088	0.078	0.144	0.141	0.134	0.141	0.135	0.133	0.148	0.148	0.128	0.144
LOI	0.94	1.46	1.36	0.62	0.37	0.12	0.27	0.60	0.06	0.15	0.21	0.36	0.06
Total	99.71	100.04	100.04	100.36	100.07	100.16	100.34	100.02	99.83	100.12	100.16	100.46	99.67
Mg#	0.61	0.61	0.59	0.55	0.55	0.52	0.51	0.53	0.51	0.51	0.51	0.56	0.56
Trace element (ppm):													
Li	4.5	5.8	4.8	5.4	4.3	3.6	4.9	4.2	4.1	4.7	3.4	3.7	3.8
Be	0.28	0.31	0.31	0.43	0.45	0.44	0.31	0.22	0.41	0.48	0.48	0.38	0.41
Rb	1.18	1.92	10.74	3.62	3.00	3.58	1.59	1.37	4.38	4.25	4.62	3.95	2.05
Sb	0.038	0.074	0.064	0.118	0.139	0.051	0.041	0.054	0.053	0.060	0.046	0.037	0.043
Cs	0.030	0.028	0.199	0.057	0.040	0.052	0.050	0.020	0.037	0.027	0.082	0.041	0.022
Pb	0.19	0.33	0.69	0.12	0.13	0.33	0.39	0.23	0.61	0.51	0.32	0.25	0.27
Sc	40.9	43.3	39.3	36.0	43.7	42.2	43.5	45.8	42.8	46.3	40.5	47.9	48.7
V	298.5	273.8	297.9	281.3	365.1	345.5	268.3	345.7	307.1	336.3	304.9	303.1	306.9
Cr	420.4	393.3	365.4	189.3	220.9	201.8	482.4	209.2	180.4	190.1	186.9	299.3	335.5
Co	48.6	48.6	46.8	44.3	47.6	47.2	51.5	47.1	43.7	43.6	46.2	47.4	51.3
Ni	157.4	144.5	152.4	90.6	109.5	97.6	186.6	95.0	83.3	89.5	82.8	106.9	120.0
Cu	117.0	176.8	160.9	154.3	154.0	160.9	132.3	191.5	167.5	170.3	163.0	148.0	145.0
Zn	78.4	63.7	78.5	75.6	105.8	103.6	74.5	83.5	89.1	96.6	85.5	85.2	90.7
Ga	16.6	15.3	16.6	16.2	18.9	18.5	14.6	17.3	17.1	19.1	16.9	17.0	16.3
Sr	157.1	144.6	197.6	171.2	196.7	173.3	148.0	187.1	165.8	178.1	172.6	166.0	164.9
Y	14.8	17.6	15.4	20.9	23.1	21.8	15.9	23.3	21.9	23.3	23.0	21.9	21.5
Ba	24.2	55.1	63.5	81.8	105.6	52.8	42.0	87.0	59.5	81.3	51.8	51.4	47.3
La	3.48	5.20	4.39	6.71	7.06	7.41	4.37	7.08	7.04	7.17	7.43	6.80	6.56
Ce	8.71	12.10	10.92	15.91	16.91	16.69	10.71	16.62	16.10	16.98	17.92	14.26	15.62
Pr	1.12	1.68	1.42	2.27	2.39	2.34	1.54	2.42	2.29	2.45	2.54	2.13	2.23
Nd	5.36	8.21	6.84	10.68	11.51	11.41	7.49	11.60	11.20	11.61	12.04	10.31	10.58
Sm	1.63	2.32	1.98	3.01	3.20	3.18	2.16	3.30	3.07	3.31	3.34	2.86	2.97
Eu	0.66	0.95	0.77	1.13	1.07	1.18	0.84	1.19	1.12	1.23	1.25	1.06	1.09
Gd	1.82	2.85	2.28	3.59	3.51	3.60	2.64	3.98	3.39	3.95	4.02	3.13	3.48
Tb	0.34	0.50	0.42	0.63	0.62	0.65	0.47	0.70	0.61	0.70	0.69	0.58	0.62
Dy	2.13	3.09	2.56	3.87	3.93	4.01	2.90	4.25	3.80	4.21	4.35	3.62	3.87
Ho	0.44	0.64	0.52	0.80	0.81	0.81	0.60	0.87	0.77	0.87	0.88	0.73	0.78
Er	1.27	1.82	1.55	2.31	2.36	2.34	1.75	2.55	2.22	2.52	2.59	2.12	2.25
Tm	0.20	0.29	0.24	0.35	0.37	0.37	0.27	0.39	0.35	0.39	0.40	0.33	0.35
Yb	1.24	1.79	1.48	2.19	2.29	2.34	1.63	2.40	2.16	2.41	2.46	2.08	2.19
Lu	0.18	0.26	0.22	0.33	0.34	0.34	0.25	0.36	0.32	0.36	0.37	0.30	0.32
Zr	48.2	69.6	61.4	87.3	105.0	106.8	68.4	95.5	94.7	106.0	108.1	85.5	88.4
Nb	5.1	6.6	6.5	9.2	11.3	11.5	6.6	10.5	10.7	11.0	11.2	9.4	9.6
Hf	1.21	1.71	1.52	2.40	2.57	2.59	1.54	2.52	2.37	2.55	2.60	2.30	2.17
Ta	0.30	0.41	0.37	0.61	0.68	0.71	0.44	0.63	0.64	0.67	0.66	0.58	0.61
Th	0.43	0.57	0.57	0.83	0.95	1.00	0.57	0.81	0.89	0.82	0.86	0.80	0.70
U	0.11	0.18	0.15	0.23	0.26	0.26	0.16	0.23	0.24	0.24	0.24	0.22	0.21

Table T2 (continued).

Core, section:	34R-3	36R-1	37R-1	38R-1	33R-2	41R-1	42R-2	43R-4
Interval (cm):	117–122	73–76	63–67	31–36	87–91	19–24	18–22	56–60
Unit:	4B-6	4B-6	4B-7	4B-7	4B-7	4B-7	4B-7	4B-7
Depth (mbsf):	556.6	563.23	566.63	573.11	579.51	585.99	591.58	599.74
Major element oxide (wt%):								
SiO_2	48.65	49.33	48.68	49.08	49.48	49.54	49.12	48.82
TiO_2	1.434	1.533	1.519	1.485	1.564	1.505	1.576	1.470
Al_2O_3	15.79	15.66	15.22	15.25	15.45	15.04	15.01	15.16
Fe_2O_{3T}	12.09	12.06	12.24	11.93	11.95	12.48	12.53	12.21
FeOT	10.88	10.86	11.01	10.74	10.75	11.23	11.28	10.99
MnO	0.181	0.184	0.149	0.194	0.184	0.207	0.202	0.186
MgO	6.88	6.65	7.26	7.23	6.65	7.10	7.02	7.15
CaO	12.45	12.56	11.65	12.07	12.65	12.41	12.26	12.36
Na_2O	2.12	2.44	2.55	2.22	2.20	2.26	2.25	2.15
K_2O	0.22	0.14	0.38	0.15	0.17	0.19	0.20	0.21
P_2O_5	0.134	0.145	0.130	0.118	0.134	0.128	0.130	0.125
LOI	0.07	0.28	0.32	0.46	0.10	–0.11	–0.12	–0.08
Total	100.02	100.98	100.08	100.19	100.53	100.74	100.18	99.75
Mg#	0.53	0.52	0.54	0.55	0.52	0.53	0.53	0.54
Trace element (ppm):								
Li	4.3	3.6	4.3	3.5	3.8	3.9	3.6	4.0
Be	0.42	0.39	0.42	0.39	0.41	0.43	0.43	0.42
Rb	3.80	1.73	8.60	3.24	6.02	3.72	3.71	4.19
Sb	0.050	0.044	0.064	0.052	0.051	0.050	0.053	0.058
Cs	0.025	0.017	0.130	0.074	0.083	0.034	0.031	0.041
Pb	0.52	0.31	0.81	0.25	0.46	0.32	0.35	0.53
Sc	43.7	40.8	48.1	50.1	49.3	48.1	42.1	47.0
V	309.7	325.5	350.8	345.2	342.0	318.6	319.0	323.9
Cr	212.8	206.5	282.0	293.5	265.8	260.9	206.0	271.7
Co	43.8	48.3	50.3	45.8	45.2	45.4	44.6	45.7
Ni	97.8	95.6	102.1	100.5	97.1	93.0	94.1	100.7
Cu	152.9	178.1	158.8	160.1	170.1	159.2	168.7	168.1
Zn	85.3	86.0	54.3	93.4	85.2	92.4	87.1	91.7
Ga	16.3	17.7	18.5	19.8	18.1	17.7	17.2	17.1
Sr	176.3	171.0	212.5	165.7	178.7	164.5	163.0	174.6
Y	21.8	23.6	24.4	23.6	24.5	24.7	23.2	23.1
Ba	56.0	56.0	163.2	43.8	46.9	52.8	55.4	50.0
La	6.63	6.36	6.89	7.11	6.80	6.39	6.77	6.09
Ce	15.56	15.15	16.37	17.05	16.78	15.62	16.55	15.03
Pr	2.22	2.19	2.35	2.34	2.38	2.35	2.35	2.18
Nd	10.54	10.54	11.22	11.29	11.63	11.27	11.18	10.68
Sm	3.01	2.98	3.23	3.23	3.32	3.29	3.32	3.05
Eu	1.06	1.06	1.16	1.16	1.20	1.19	1.14	1.08
Gd	3.49	3.47	3.86	3.52	3.91	3.89	3.73	3.52
Tb	0.61	0.60	0.66	0.66	0.70	0.69	0.66	0.62
Dy	3.75	3.66	4.03	4.03	4.25	4.27	4.10	3.92
Ho	0.78	0.78	0.83	0.82	0.88	0.89	0.84	0.80
Er	2.27	2.18	2.28	2.32	2.54	2.56	2.45	2.32
Tm	0.35	0.34	0.35	0.36	0.39	0.39	0.38	0.35
Yb	2.15	2.14	2.16	2.19	2.40	2.45	2.38	2.24
Lu	0.33	0.32	0.32	0.32	0.36	0.36	0.35	0.33
Zr	86.3	85.0	44.8	90.8	98.5	100.4	100.9	102.9
Nb	9.7	9.6	9.8	9.4	9.9	10.3	10.3	9.2
Hf	2.16	2.23	1.57	2.35	2.42	2.41	2.38	2.52
Ta	0.56	0.57	0.62	0.60	0.55	0.57	0.58	0.60
Th	0.71	0.69	0.56	0.69	0.76	0.75	0.77	0.75
U	0.20	0.20	0.12	0.19	0.23	0.24	0.24	0.23

Table T3. INA analysis of Subunits 4A and 4B, Sites 1039 and 1040.

Hole:	1039C	1039C	1039C	1039C	1039C	1039C	1039C	1039C	1039C	1039C	1039C	1039C	1040C	1040C	1040C	1040C
Core, section:	7R-2	7R-3	8R-1	8R-3	8R-4	8R-5	9R-1	10R-1	10R-2	10R-3	11R-1	11R-1	52R-4	52R-4	53R-1	53R-1
Interval (cm):	72–75	126–129	79–82	34–37	81–84	18–21	81–84	30–33	122–125	59–61	17–19	55–58	19–22	37–41	50–52	118–121
Unit:	4A	4A	4A	4A	4A	4A	4A	4A	4A	4A	4B	4B	4B	4B	4B	4B
Depth (mbsf):	422.5	424.5	431.1	432.6	434.2	434.9	436.5	440.2	441.5	442.9	443.2	443.6	653.8	654	660.1	660.8
Major element oxide (wt%):																
FeO	11.51	10.99	11.04	11.25	11.17	11.53	11.18	11.41	11.34	11.43	11.73	11.37	10.54	10.34	11.53	11.21
CaO	11.3	12	12.1	11.8	12.2	12.1	12.9	12.7	12.6	13.1	12.5	13.4	13.3	13.6	12.4	12.8
Na_2O	2.53	2.47	2.42	2.42	2.56	2.33	2.34	2.41	2.36	2.39	2.35	2.29	2.24	2.29	2.56	2.52
Trace element (ppm):																
Zr	130	140	130	160	120	140	130	150	160	120	<120	130	<170	160	130	150
Sr	200	240	220	240	210	210	240	250	240	210	170	200	210	160	170	220
Cr	260	247	136.6	232	283	281	256	260	264	254	167.2	168.5	207	202	177.8	179.9
Ba	198	90	106	96	152	107	137	90	78	74	73	51	46	41	46	42
Sc	42.3	41.3	37.7	40.1	41.2	42	40.4	41.3	41.2	40.9	44.7	44.7	45.9	45.9	44.4	44.1
Co	48	46.9	42.4	45.9	45.3	48.1	46.3	47	46.8	47.8	48.4	47.4	46.3	48.4	48.9	46.4
La	14.08	14.61	14.46	14.08	13.22	14.24	13.74	14.09	14.23	14.4	8.32	8.32	6.9	6.93	7.69	7.4
Ce	32.4	33.2	32.7	31.5	30.4	31.7	30.7	31.8	32.2	32.3	19.3	19.2	15.4	15.9	18.7	18.1
Nd	17	17	19	17	17	18	19	20	20	20	15	11	12	12	15	10
Sm	4.91	5.03	4.97	4.8	4.8	4.71	4.73	4.9	4.95	4.96	3.54	3.58	3.03	3.06	3.63	3.62
Eu	1.56	1.66	1.62	1.58	1.56	1.62	1.58	1.62	1.63	1.64	1.25	1.26	1.1	1.11	1.31	1.26
Tb	0.9	0.99	0.95	0.93	0.89	0.92	0.9	0.86	0.92	0.94	0.8	0.76	0.68	0.65	0.76	0.73
Yb	2.75	2.82	2.77	2.7	2.74	2.77	2.61	2.7	2.78	2.76	2.66	2.66	2.38	2.43	2.55	2.6
Lu	0.397	0.414	0.418	0.402	0.393	0.405	0.395	0.401	0.414	0.404	0.39	0.406	0.35	0.355	0.386	0.391
Hf	3.88	3.83	3.86	3.73	3.7	3.74	3.63	3.74	3.84	3.89	2.66	2.67	2.17	2.14	2.68	2.53
Ta	1.15	1.13	1.17	1.12	1.06	1.12	1.09	1.09	1.11	1.12	0.61	0.62	0.48	0.5	0.58	0.58
Th	1.44	1.41	1.47	1.42	1.36	1.39	1.31	1.41	1.4	1.42	0.83	0.85	0.67	0.7	0.65	0.66
U	0.37	0.4	0.5	0.38	0.35	0.5	<1.0	0.37	0.42	0.59	0.33	<0.6	0.26	0.46	<0.6	<0.5